Engineering Geology 374 (2026) 109124

Contents lists available at ScienceDirect

Engineering Geology

journal homepage: www.elsevier.com/locate/enggeo

The infiltration paradox: Pore-gas pressure controls on early slope failure during rapid hydraulic loading

Xiaoying Chen [a], Jidong Zhao [a,*], Jidu Yu [a,b]

[a] Department of Civil and Environmental Engineering, Hong Kong University of Science and Technology, Hong Kong, China
[b] Department of Civil and Environmental Engineering, University of California, Berkeley, USA

ARTICLE INFO

Keywords:
Unsaturated slope stability
Pore-gas pressure
Rapid inundation
Three-phase coupling
Material point method

ABSTRACT

The assumption of atmospheric pore-gas pressure in slope stability analysis can break down under rapid surface hydraulic loading, such as flash floods or wave overtopping. In these events, transient water heads build up faster than the internal groundwater system can equilibrate, trapping and compressing pore-air and altering the effective stress regime. This study examines the role of evolving pore-gas pressure on the timing of slope failure using a three-phase hydro-mechanical material point method (MPM) that couples large deformation with immiscible water-gas flow. We simulate a partially saturated slope subjected to a transient surface water head increase, comparing predictions from the fully gas-coupled model against a reference model in which pore-gas pressure remains fixed at atmospheric levels. The simulations reveal a distinct regime shift in failure behaviour. Under weak loading, both models predict similar failure onset times. Under strong loading, resolving gas evolution leads to progressively earlier instability, with a maximum difference of about 6 s at a surface head of 2.5 m. Sensitivity analysis confirms that the crossover between the two predictions is configuration dependent rather than a universal threshold. Because the 2.5 m case involves severe loading and restricted surface venting, the difference represents an upper bound for the present model configuration. Notably, earlier failure occurs even though gas coupling retards wetting and produces a shallower wetting front, a counterintuitive outcome termed the "infiltration paradox". Gas compression and redistribution increase the phase-weighted mixture pressure within the developing shear band, shifting the effective stress path towards earlier localization. These findings clarify when evolving pore-gas pressure may materially affect failure timing under rapid hydraulic loading.

1. Introduction

Slope instability in partially saturated soils is commonly explained by wetting front advance, loss of matric suction, rising pore-water pressure, and the associated reduction in shear resistance (Iverson, 2000; Alonso et al., 2003). This water-centred framework has explained many rainfall-induced failures, but it can understate the role of pore-gas. Water and gas share the pore space of an unsaturated soil. Water entry must therefore be accompanied by gas displacement, compression, or venting. When gas escape is restricted, the hydraulic response involves coupled interactions among the soil skeleton, pore-water, and pore-gas (Touma and Vauclin, 1986; Hu et al., 2011; Cho, 2016).

Recent experiments show that the influence of pore-gas is conditional rather than universal. It depends on how rapidly water enters the soil and how readily gas can escape. Wang et al. (2023) observed that intense rainfall can form a transient saturated layer near the ground surface. Gas beneath this layer becomes temporarily confined and compressed, allowing pressure to propagate into deeper soil and contribute to shallow deformation. By contrast, the centrifuge tests of Cho et al. (2024) recorded only small pore-gas pressure changes when air was displaced effectively during rainfall. Pore-water pressure remained the principal trigger of failure. Liang et al. (2026) further demonstrated that restricted venting generates substantially higher pore-gas pressure and retards wetting front advance relative to an open boundary. Pore-gas may also contribute directly to instability. Kang and Yue (2023) showed that a small volume of pressurized gas trapped beneath a low permeability layer could trigger failure in an otherwise stable gentle slope. Together, these studies reveal a dual role: pore-gas can resist water invasion and delay wetting, yet elevated gas pressure can also alter effective stress and promote failure.

This dual role becomes particularly relevant under rapid surface hydraulic loading. Conventional rainfall-induced groundwater rise does not represent all important failure scenarios. Overtopping, flooding above a slope, crest ponding, and rapid water level rise can impose

* Corresponding author.
E-mail addresses: xchenjm@connect.ust.hk (X. Chen), jzhao@ust.hk (J. Zhao), jyubu@connect.ust.hk (J. Yu).

https://doi.org/10.1016/j.enggeo.2026.109124
Received 26 May 2026; Received in revised form 13 September 2026; Accepted 3 October 2026
Available online 8 October 2026
0013-7952/© 2026 Elsevier B.V. All rights are reserved, including those for text and data mining, AI training, and similar technologies.

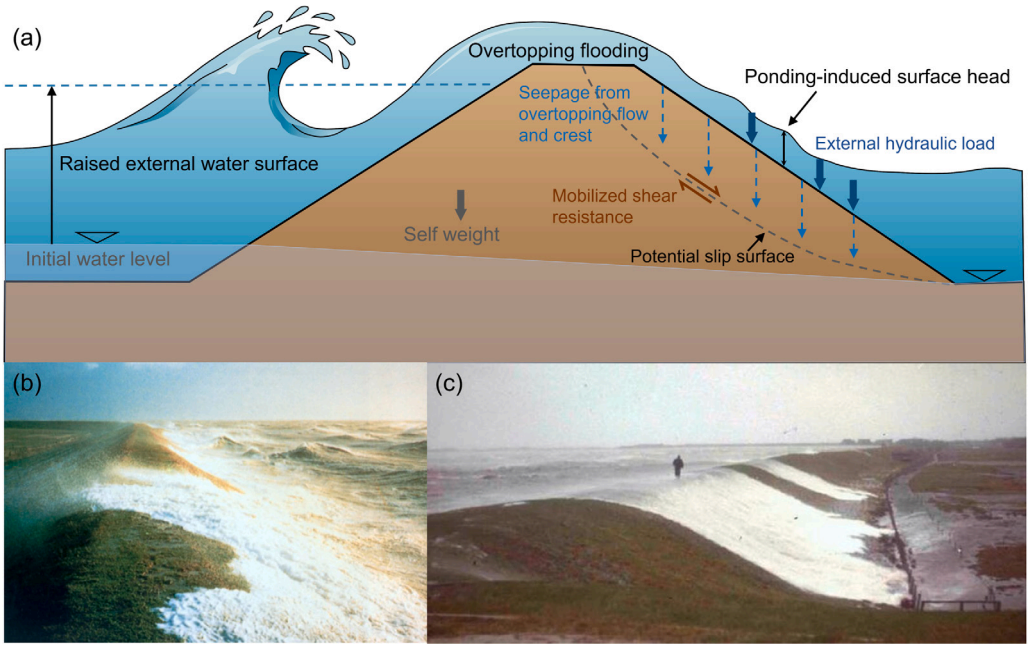


Fig. 1. Representative rapid surface-hydraulic loading scenarios for partially saturated slopes and embankments. (a) Conceptual illustration of overtopping-induced loading and the principal actions on a potential sliding mass, including self-weight, external hydraulic loading, seepage from overtopping and crest ponding, mobilized shear resistance, and the potential slip surface. Adapted conceptually from Johnston et al. (2021) and Zhou et al. (2022); (b) Wave overtopping of a grass-covered dike at Hartlepool, UK (from Warmink et al. (2018)); (c) Wave overtopping over a grass-covered sea dike in Germany (from van Bergeijk (2022)).

an external head faster than the internal water and gas pressures can equilibrate. The ground surface may become submerged while the phreatic surface inside the slope remains relatively low. Under these conditions, the rapid increase in water pressure can compress gas ahead of the advancing wetting front. Johnston et al. (2021) identified overtopping and flooding above slopes as important modes of flood-induced embankment weakening. Large-scale experiments by Zhou et al. (2022) further showed that landslide dam failure may involve coupled overtopping and seepage, with the upstream water head acting as a major destabilizing factor. Fig. 1a summarizes these loading conditions and the principal actions on a potential sliding mass, including self-weight, external hydraulic loading, seepage, and mobilized shear resistance. Fig. 1b and c show representative dike overtopping conditions reported by Warmink et al. (2018) and van Bergeijk (2022). The numerical problem considered here therefore represents a generic earth embankment or engineered soil slope subjected to rapid overtopping or crest ponding before its internal pore system reaches hydraulic equilibrium.

Modelling the resulting transition from transient multiphase flow to large slope deformation requires a method that can describe both pore pressure evolution and post-failure motion. The Material Point Method (MPM) is well suited to this task because it combines Lagrangian material points with a fixed computational grid and avoids the mesh distortion associated with large deformation. Yerro et al. (2015) introduced a fully dynamic three-phase single-point MPM for unsaturated soil. Subsequent work has advanced time integration, phase representation, hydraulic boundary treatment, constitutive modelling, and experimental validation (Yerro et al., 2022; Ceccato et al., 2024). Lei et al. (2021) extended GIMP to coupled problems in unsaturated soil, Hidano et al. (2024) developed a semi-implicit formulation for infiltration-induced failure, and Di Carluccio et al. (2025) reproduced wetting collapse, failure, and deposition of an unsaturated slope. These slope applications, however, neglect pore-gas evolution or prescribe pore-gas pressure as atmospheric. Higo et al. (2025) recently proposed a three-phase two-point MPM that explicitly resolves the gas phase during large deformation, but its demonstrated application focused on seismic liquefaction. Thus, despite substantial progress in multiphase MPM, the influence of evolving compressible pore-gas on slope failure timing under rapid surface hydraulic loading remains poorly quantified.

The available evidence therefore presents a sharp but unresolved contrast. Pore-gas can retard wetting, yet sufficiently high gas pressure can accelerate instability (Kang and Yue, 2023; Liang et al., 2026). It remains unclear when pore-gas pressure acts mainly as a passive response to wetting and deformation, and when it becomes an active control on failure timing. More fundamentally, it is unclear how a slope can fail earlier while its wetting front remains shallower. Previous studies have generally examined hydraulic retardation and gas-induced destabilization as separate processes. A unified explanation linking loading intensity, phase pressure partitioning, and the effective stress path within an evolving shear band is still lacking. We term this counterintuitive response the "infiltration paradox". Here, infiltration refers broadly to wetting progression and water penetration rather than specifically the water flux entering the ground surface.

To address this gap, we propose a three-phase hydro-mechanical (HM) MPM that explicitly resolves the coupled evolution of the soil skeleton, pore-water, and compressible pore-gas. Unlike models that neglect gas evolution or prescribe pore-gas pressure as atmospheric, the present formulation solves the gas mass and momentum balances and updates pore-gas pressure in space and time. The novelty therefore lies not simply in adopting a three-phase formulation, but in determining when explicit gas pressure becomes necessary and explaining how it changes failure timing under rapid hydraulic loading. Simulations with evolving pore-gas pressure are compared directly with a reference model in which pore-gas pressure remains atmospheric. The imposed surface water head is varied from zero to 2.5 m. The upper end of this range represents severe short-duration loading with restricted surface venting rather than a typical rainfall condition. The analysis quantifies failure onset, wetting front advance, liquid and gas contributions to mixture pressure, effective stress evolution, and strain localization. For the reference configuration, the ordering of the two onset predictions changes over a narrow head interval near 0.5–0.7 m. Appendix shows that this crossover shifts substantially with the hydraulic properties,

initial state, and surface gas boundary, and should therefore not be interpreted as a universal threshold. The results further show that gas compression and redistribution can modify the shear band stress path and advance failure even when the wetting front remains shallower.

2. Governing equations

The unsaturated porous medium is represented as three overlapping continua: the solid skeleton, pore-liquid, and pore-gas. The liquid and gas phases are immiscible and have independent velocity and pressure fields. Phase change and mass transfer between the two fluids are neglected (Coussy, 2004a; de la Cruz et al., 1993; Lei et al., 2021). The solid grains are assumed incompressible, the liquid phase is weakly compressible, and the gas phase is compressible and follows the ideal gas law (Ye et al., 2022; Coussy, 2004a; Zienkiewicz and Shiomi, 1984). Fluid motion relative to the skeleton is governed by Darcy's law, and the contribution of the pore pressures to the skeleton stress is described using Bishop's effective stress. All processes are assumed isothermal.

Unless otherwise stated, P_l and P_g denote pressures relative to the atmospheric reference pressure P_atm. The ideal gas relation uses the absolute pore-gas pressure $P_\mathrm{g}^\mathrm{abs} = P_\mathrm{g} + P_\mathrm{atm}$.

2.1. Phase description

Consider a representative elementary volume V, composed of the partial volumes of the solid, liquid, and gas phases (Ehlers, 2002; Yerro et al., 2015), i.e.,

$$V = \sum_\pi V_\pi = V_\mathrm{s} + V_\mathrm{l} + V_\mathrm{g}, \qquad \pi = \mathrm{s}, \mathrm{l}, \mathrm{g}, \tag{1}$$

where V_π is the partial volume of phase π, and the subscripts s, l, and g denote the solid, liquid, and gas phases, respectively. The porosity n, defined as the fraction of the total volume occupied by the fluids, is

$$n = \frac{V_\mathrm{l} + V_\mathrm{g}}{V}, \tag{2}$$

The liquid and gas saturations are

$$S_\mathrm{l} = \frac{V_\mathrm{l}}{V_\mathrm{l} + V_\mathrm{g}}, \qquad S_\mathrm{g} = 1 - S_\mathrm{l}. \tag{3}$$

The phase volume fractions can be written as $n_\mathrm{s} = 1 - n$, $n_\mathrm{l} = nS_\mathrm{l}$, and $n_\mathrm{g} = nS_\mathrm{g}$. The bulk density of the three-phase medium is obtained by volume averaging of the intrinsic phase densities (Whitaker, 1986):

$$\rho = \sum_\pi n_\pi \rho_\pi = (1-n)\rho_\mathrm{s} + nS_\mathrm{l}\rho_\mathrm{l} + nS_\mathrm{g}\rho_\mathrm{g}, \tag{4}$$

where ρ_s, ρ_l, and ρ_g are the intrinsic densities of the solid, liquid, and gas phases, respectively.

2.2. Conservation of mass

The intrinsic density of the solid phase is constant. The weak compressibility of the liquid is described by

$$\frac{1}{\rho_\mathrm{l}}\frac{D^\mathrm{s}\rho_\mathrm{l}}{Dt} = \frac{1}{K_\mathrm{l}}\frac{D^\mathrm{s}P_\mathrm{l}}{Dt}, \tag{5}$$

where K_l is the liquid bulk modulus.

Let $D^\pi(\cdot)/Dt$ denote the material derivative following phase π. The pore-gas density satisfies the ideal gas law,

$$\rho_\mathrm{g} = \frac{P_\mathrm{g}^\mathrm{abs} M_\mathrm{g}}{RT}, \tag{6}$$

where M_g is the molar mass of pore-gas, R is the universal gas constant, and T is the absolute temperature.

Mass conservation of the solid phase is written as

$$\frac{D^\mathrm{s}\left[(1-n)\rho_\mathrm{s}\right]}{Dt} + (1-n)\rho_\mathrm{s}\nabla\cdot\mathbf{v}_\mathrm{s} = 0, \tag{7}$$

where $\mathbf{v}_\mathrm{s}$ is the solid velocity.

For each fluid phase $\alpha = \mathrm{l}, \mathrm{g}$, mass conservation relative to the moving skeleton is (Lei et al., 2021; Zienkiewicz and Shiomi, 1984):

$$\frac{D^\mathrm{s}\left(nS_\alpha\rho_\alpha\right)}{Dt} + nS_\alpha\rho_\alpha\nabla\cdot\mathbf{v}_\mathrm{s} + \nabla\cdot\left[nS_\alpha\rho_\alpha\left(\mathbf{v}_\alpha - \mathbf{v}_\mathrm{s}\right)\right] = 0, \qquad \alpha = \mathrm{l}, \mathrm{g}, \tag{8}$$

The relative volumetric flux of phase α is defined as

$$\mathbf{J}_\alpha = nS_\alpha\left(\mathbf{v}_\alpha - \mathbf{v}_\mathrm{s}\right), \qquad \alpha = \mathrm{l}, \mathrm{g}, \tag{9}$$

The liquid saturation is treated as a function of capillary pressure, $P_\mathrm{c} = P_\mathrm{g} - P_\mathrm{l}$. Assuming that the spatial variation of the intrinsic liquid density within a representative volume is negligible, combining Eqs. (8) and (5) gives

$$n\frac{D^\mathrm{s}P_\mathrm{l}}{Dt}\left(\frac{S_\mathrm{l}}{K_\mathrm{l}} + \frac{\partial S_\mathrm{l}}{\partial P_\mathrm{l}}\right) - n\frac{D^\mathrm{s}P_\mathrm{g}}{Dt}\frac{\partial S_\mathrm{l}}{\partial P_\mathrm{l}} + S_\mathrm{l}\nabla\cdot\mathbf{v}_\mathrm{s} + \nabla\cdot\mathbf{J}_\mathrm{l} = 0, \tag{10}$$

where $S_\mathrm{g} = 1 - S_\mathrm{l}$.

Similarly, assuming a negligible intrinsic gas density gradient within the representative volume and substituting Eq. (6) into Eq. (8), the gas mass balance becomes

$$n\frac{D^\mathrm{s}P_\mathrm{g}}{Dt}\left(\frac{S_\mathrm{g}M_\mathrm{g}}{\rho_\mathrm{g}RT} + \frac{\partial S_\mathrm{l}}{\partial P_\mathrm{l}}\right) - n\frac{D^\mathrm{s}P_\mathrm{l}}{Dt}\frac{\partial S_\mathrm{l}}{\partial P_\mathrm{l}} + S_\mathrm{g}\nabla\cdot\mathbf{v}_\mathrm{s} + \nabla\cdot\mathbf{J}_\mathrm{g} = 0. \tag{11}$$

Eqs. (10) and (11) describe the coupled evolution of pore-water and pore-gas pressures. The coupling arises from skeleton deformation, saturation change, relative fluid transport, liquid compressibility, and gas compressibility.

2.3. Conservation of momentum

The momentum balances of the liquid and gas phases account for inertia, pressure gradients, gravity, and drag exerted by the solid skeleton (Lei et al., 2021; Roth and Aydogan, 2015)

$$nS_\mathrm{l}\rho_\mathrm{l}\mathbf{a}_\mathrm{l} = -nS_\mathrm{l}\nabla P_\mathrm{l} + nS_\mathrm{l}\mathbf{f}_\mathrm{l} + nS_\mathrm{l}\rho_\mathrm{l}\mathbf{b}, \tag{12}$$

$$nS_\mathrm{g}\rho_\mathrm{g}\mathbf{a}_\mathrm{g} = -nS_\mathrm{g}\nabla P_\mathrm{g} + nS_\mathrm{g}\mathbf{f}_\mathrm{g} + nS_\mathrm{g}\rho_\mathrm{g}\mathbf{b}, \tag{13}$$

where $\mathbf{a}_\alpha$ is the acceleration of phase α, $\mathbf{b}$ is the gravitational acceleration vector, and $\mathbf{f}_\alpha$ is the drag interaction force per unit volume between phase α and the solid skeleton. The drag interaction is closed using Darcy's law for laminar flow through a porous skeleton

$$\mathbf{f}_\mathrm{l} = -\frac{\mu_\mathrm{l}}{k_\mathrm{a}k_\mathrm{rl}}\mathbf{J}_\mathrm{l} = -\frac{nS_\mathrm{l}\mu_\mathrm{l}}{k_\mathrm{a}k_\mathrm{rl}}\left(\mathbf{v}_\mathrm{l} - \mathbf{v}_\mathrm{s}\right), \tag{14}$$

$$\mathbf{f}_\mathrm{g} = -\frac{\mu_\mathrm{g}}{k_\mathrm{a}k_\mathrm{rg}}\mathbf{J}_\mathrm{g} = -\frac{nS_\mathrm{g}\mu_\mathrm{g}}{k_\mathrm{a}k_\mathrm{rg}}\left(\mathbf{v}_\mathrm{g} - \mathbf{v}_\mathrm{s}\right), \tag{15}$$

where k_a is the absolute permeability, $k_{\mathrm{r}\alpha}$ is the relative permeability, and μ_α is the dynamic viscosity; μ_α is assumed to be weakly dependent on state variables and is thus treated as constant.

The momentum balance of the complete mixture is (Bandara et al., 2016; Schrefler and Scotta, 2001)

$$(1-n)\rho_\mathrm{s}\mathbf{a}_\mathrm{s} + nS_\mathrm{l}\rho_\mathrm{l}\mathbf{a}_\mathrm{l} + nS_\mathrm{g}\rho_\mathrm{g}\mathbf{a}_\mathrm{g} = \nabla\cdot\boldsymbol{\sigma} + \rho\mathbf{b}, \tag{16}$$

where $\mathbf{a}_\mathrm{s}$ is the acceleration of the solid skeleton, $\rho = (1-n)\rho_\mathrm{s} + nS_\mathrm{l}\rho_\mathrm{l} + nS_\mathrm{g}\rho_\mathrm{g}$ is the mixture density, and $\boldsymbol{\sigma}$ is the total Cauchy stress tensor. Following Bishop's effective stress concept (Bandara et al., 2016; Lu and Likos, 2004), the total stress is decomposed as

$$\boldsymbol{\sigma} = \boldsymbol{\sigma}' - \left(\chi_\mathrm{l}P_\mathrm{l} + \chi_\mathrm{g}P_\mathrm{g}\right)\mathbf{I}, \tag{17}$$

where $\boldsymbol{\sigma}'$ is the effective stress tensor, $\mathbf{I}$ is the second-order identity tensor, and χ_l, χ_g are Bishop weighting coefficients for the liquid and gas pressures. In the present study, they are taken as saturation-based weights satisfying $\chi_\mathrm{l} + \chi_\mathrm{g} = 1$

$$\chi_\mathrm{l} = \frac{S_\mathrm{l}}{S_\mathrm{l} + S_\mathrm{g}}, \tag{18}$$

$$\chi_{\mathrm{g}} = \frac{S_{\mathrm{g}}}{S_{\mathrm{l}} + S_{\mathrm{g}}}. \tag{19}$$

Eqs. (12)–(16) form a coupled momentum system. Darcy drag links the fluid velocities to the solid motion, while the mixture equation enforces overall momentum balance. In the numerical implementation adopted in this study, the three-phase accelerations are obtained from a local coupled nodal solution rather than from independent phase updates.

2.4. Boundary conditions

The three-phase mixture occupies a spatial domain Ω with boundary $\partial\Omega$. Boundary conditions are specified in terms of Dirichlet conditions for the primary variables and Neumann conditions for the corresponding tractions or phase fluxes. Specifically, Dirichlet boundaries prescribe the phase velocities on $\partial\Omega_{v_{\mathrm{s}}}$, $\partial\Omega_{v_{\mathrm{l}}}$, and $\partial\Omega_{v_{\mathrm{g}}}$, and the pore pressures on $\partial\Omega_{P_{\mathrm{l}}}$ and $\partial\Omega_{P_{\mathrm{g}}}$. Neumann boundaries prescribe the traction $\bar{\mathbf{t}}(t)$ on $\partial\Omega_t$, and the liquid and gas fluxes $\bar{q}_{\mathrm{l}}(t)$ and $\bar{q}_{\mathrm{g}}(t)$ on $\partial\Omega_{q_{\mathrm{l}}}$ and $\partial\Omega_{q_{\mathrm{g}}}$, respectively. The boundary conditions are written as

$$\mathbf{v}_{\mathrm{s}}(\mathbf{x},t) = \bar{\mathbf{v}}_{\mathrm{s}}(t) \quad \text{on } \partial\Omega_{v_{\mathrm{s}}} \tag{20}$$

$$\mathbf{v}_{\mathrm{l}}(\mathbf{x},t) = \bar{\mathbf{v}}_{\mathrm{l}}(t) \quad \text{on } \partial\Omega_{v_{\mathrm{l}}} \tag{21}$$

$$\mathbf{v}_{\mathrm{g}}(\mathbf{x},t) = \bar{\mathbf{v}}_{\mathrm{g}}(t) \quad \text{on } \partial\Omega_{v_{\mathrm{g}}} \tag{22}$$

$$P_{\mathrm{l}}(\mathbf{x},t) = \bar{P}_{\mathrm{l}}(t) \quad \text{on } \partial\Omega_{P_{\mathrm{l}}} \tag{23}$$

$$P_{\mathrm{g}}(\mathbf{x},t) = \bar{P}_{\mathrm{g}}(t) \quad \text{on } \partial\Omega_{P_{\mathrm{g}}} \tag{24}$$

$$\boldsymbol{\sigma}(\mathbf{x},t)\cdot\mathbf{n} = \bar{\mathbf{t}}(t) \quad \text{on } \partial\Omega_t \tag{25}$$

$$\mathbf{J}_{\mathrm{l}}(\mathbf{x},t)\cdot\mathbf{n} = -\bar{q}_{\mathrm{l}}(t) \quad \text{on } \partial\Omega_{q_{\mathrm{l}}} \tag{26}$$

$$\mathbf{J}_{\mathrm{g}}(\mathbf{x},t)\cdot\mathbf{n} = -\bar{q}_{\mathrm{g}}(t) \quad \text{on } \partial\Omega_{q_{\mathrm{g}}} \tag{27}$$

where $\mathbf{n}$ is the outward unit normal vector on $\partial\Omega$. Here, the prescribed fluxes $\bar{q}_{\mathrm{l}}(t)$ and $\bar{q}_{\mathrm{g}}(t)$ represent boundary fluxes of liquid and gas, respectively. These flux boundary conditions are expressed in terms of the relative volumetric flux $\mathbf{J}_\alpha = nS_\alpha(\mathbf{v}_\alpha - \mathbf{v}_{\mathrm{s}})$ introduced in Section 2.2, so that $\mathbf{J}_\alpha\cdot\mathbf{n}$ denotes the normal flux of phase α across the boundary.

At time $t = 0$, the system is initialized by $\{\mathbf{v}_{\mathrm{s}}^0, \mathbf{v}_{\mathrm{l}}^0, \mathbf{v}_{\mathrm{g}}^0, P_{\mathrm{l}}^0, P_{\mathrm{g}}^0\}$. To ensure well-posedness, Dirichlet and Neumann conditions are not imposed simultaneously on the same boundary portion, i.e. $\partial\Omega_{v_{\mathrm{s}}}\cap\partial\Omega_t = \varnothing$, $\partial\Omega_{P_{\mathrm{l}}}\cap\partial\Omega_{q_{\mathrm{l}}} = \varnothing$, $\partial\Omega_{P_{\mathrm{g}}}\cap\partial\Omega_{q_{\mathrm{g}}} = \varnothing$.

3. Constitutive models

3.1. Mechanical constitutive law

The mechanical response of the solid skeleton is described using an elastoplastic model formulated in terms of effective stress. A Mohr–Coulomb type yield criterion with a smooth approximation in the deviatoric plane is adopted to avoid the numerical singularities associated with the corners of the classical yield surface (Cui et al., 2018). The influence of partial saturation enters through the saturation-weighted Bishop effective stress defined in Eq. (17) and the coupled hydraulic variables. No separate suction-dependent yield surface is introduced.

The constitutive relation is written in rate form as

$$\dot{\boldsymbol{\sigma}}' = \mathbb{D} : \left(\dot{\boldsymbol{\varepsilon}} - \dot{\boldsymbol{\varepsilon}}^{\mathrm{p}}\right), \tag{28}$$

where $\boldsymbol{\sigma}'$ is the effective stress tensor, $\mathbb{D}$ is the elastic stiffness tensor, $\dot{\boldsymbol{\varepsilon}}$ is the total strain-rate tensor, and $\dot{\boldsymbol{\varepsilon}}^{p}$ is the plastic strain-rate tensor. Under the isothermal conditions considered here, the total strain rate is determined from the symmetric part of the solid velocity gradient:

$$\dot{\boldsymbol{\varepsilon}} = \dot{\boldsymbol{\varepsilon}}_{\mathrm{s}} = \frac{1}{2}\left[\nabla\boldsymbol{v}_{\mathrm{s}} + \left(\nabla\boldsymbol{v}_{\mathrm{s}}\right)^{T}\right], \tag{29}$$

Plastic deformation follows a non-associated flow rule. The incremental plastic strain is obtained from the plastic potential P:

$$d\boldsymbol{\varepsilon}^{\mathrm{p}} = d\lambda\frac{\partial P}{\partial\boldsymbol{\sigma}'}, \tag{30}$$

where $d\lambda$ is the plastic multiplier. Plastic loading occurs when the yield function F reaches zero and the loading condition is satisfied. The yield function F and plastic potential P are expressed in terms of the effective friction angle ϕ', cohesion c', and dilation angle ψ as

$$F = R_{\mathrm{mc}}\,q + p\tan\varphi' - c', \tag{31}$$

$$P = \sqrt{(\epsilon c'\tan\psi)^2 + \left(R_{\mathrm{mw}}q\right)^2} + p\tan\psi, \tag{32}$$

where p and q are the mean and equivalent deviatoric effective stresses, respectively; ϕ' is the effective friction angle; c' is the effective cohesion; and ψ is the dilation angle. The scalar ϵ is the meridional eccentricity that controls the smoothness of the plastic potential in the p–q plane.

The functions R_{mw} and R_{mc} represent the Lode angle dependence of the plastic potential and yield surface:

$$R_{\mathrm{mw}}(\theta,e) = \frac{4(1-e^2)\cos^2\theta + (2e-1)^2}{2(1-e^2)\cos\theta + (2e-1)\sqrt{4(1-e^2)\cos^2\theta + e(5e-4)}}\,R_{\mathrm{mc}}\left(\frac{\pi}{3},\varphi'\right), \tag{33}$$

$$R_{\mathrm{mc}}(\theta,\varphi') = \frac{1}{\sqrt{3}\cos\varphi'}\sin\left(\theta+\frac{\pi}{3}\right) + \frac{1}{3}\cos\left(\theta+\frac{\pi}{3}\right)\tan\varphi', \tag{34}$$

where θ is the Lode angle and e is the deviatoric eccentricity. These functions provide a smooth representation of the Mohr–Coulomb surface while retaining its dependence on the intermediate principal stress.

The selected formulation provides an established mechanical basis for mechanism-oriented MPM analyses of unsaturated slope failure. Comparable effective stress and Mohr–Coulomb formulations have been used to reproduce failure initiation, strain localization, and large deformation in previous MPM studies (Yerro et al., 2015; Lei et al., 2021), and Mohr–Coulomb remains widely used in MPM landslide analysis because of its transparent parameters and robust large deformation performance (Ceccato et al., 2024). In the present model, φ' is assumed independent of suction. Under this assumption, an effective stress description provides a consistent representation of unsaturated shear strength with a limited number of mechanical parameters (Sheng, 2011).

The same effective stress relation, elastic properties, strength parameters, and dilation angle are used in every simulation. The paired calculations therefore differ only in their treatment of pore-gas pressure, allowing its hydraulic and mechanical effects to be isolated. No strain hardening or softening is included, and $\psi = 0°$ is adopted consistently with the reference slope setting of Lei et al. (2021). This choice does not suppress the total volumetric deformation of the skeleton. Particle volume and porosity continue to evolve with the deformation field and remain coupled to the liquid and gas pressure updates. It excludes only the additional plastic volume change associated with shear dilation or contraction.

The present constitutive setting is intended for a controlled comparison rather than a site-specific calibration. More advanced suction-dependent or state-dependent formulations may refine the absolute predictions of strain localization, displacement, and failure timing, particularly where wetting collapse or pronounced dilative or contractive behaviour is important (Sheng, 2011; Di Carluccio et al., 2025). Accordingly, the subsequent analysis focuses on the relative response between the evolving and fixed pore-gas pressure models under otherwise identical mechanical conditions.

3.2. Hydraulic constitutive relations

To close the hydraulic system for multiphase flow in deformable unsaturated porous media, additional constitutive relations are required to link suction, saturation, and permeability. In the present work, a van Genuchten soil water retention curve (SWRC) is adopted together with saturation-dependent relative permeability functions, while the intrinsic permeability is allowed to evolve with porosity.

Using the van Genuchten retention relation (van Genuchten, 1980), the effective saturation S_e is defined as

$$S_e = \frac{S_l - S_{rl}}{1 - S_{rl} - S_{rg}} = \left[1 + \left(\frac{P_c}{P_0}\right)^{\frac{1}{1-m}}\right]^{-m}, \tag{35}$$

where S_{rl} and S_{rg} are the residual liquid and gas saturations, respectively, P_0 is a scaling pressure, and m is an empirical fitting parameter. In the numerical implementation, negative suction is not allowed, i.e., $P_c = \max(P_g - P_l, 0)$ so that the adopted SWRC is evaluated only over its physically admissible range.

The liquid saturation is then recovered from the effective saturation as

$$S_l = S_e\left(1 - S_{rl} - S_{rg}\right) + S_{rl}, \tag{36}$$

and the gas saturation is obtained from $S_g = 1 - S_l$.

For use in the mass balance equations, the derivative $\partial S_l / \partial P_l$ is evaluated consistently from the SWRC through the chain rule.

The relative permeabilities of the liquid and gas phases are expressed as functions of effective saturation (Lewis and Schrefler, 1998):

$$k_{rl} = S_e^{2m_l+3}, \tag{37}$$

$$k_{rg} = \left(1 - S_e\right)^2\left(1 - S_e^{2m_g+1}\right), \tag{38}$$

which are consistent with the permeability update implemented in the numerical model.

To account for deformation-induced porosity changes, the intrinsic permeability is corrected by a porosity factor (Sun et al., 2019; Ye et al., 2022),

$$k_\phi = \left(\frac{n}{n_0}\right)^{1.5}\left(\frac{1-n_0}{1-n}\right)^3, \tag{39}$$

so that the updated intrinsic permeability becomes $k_a = k_{a0}\, k_\phi$, where n is the current porosity, n_0 is the initial porosity, and k_{a0} is the reference intrinsic permeability. The phase permeabilities entering Darcy's law are then evaluated as $k_l = k_a\, k_{rl}$, $k_g = k_a\, k_{rg}$.

4. MPM implementation

4.1. GIMP discretization

The coupled HM system for the three-phase medium, comprising the pressure evolution equations, Eqs. (10)–(11), and the phase-wise and mixture momentum balances, Eqs. (12)–(13) and (16), is discretized using the Generalized Interpolation Material Point (GIMP) method (Gu et al., 2016; Lei et al., 2021; Yu et al., 2024). The primary kinematic unknowns are the phase velocities $\mathbf{v}_s$, $\mathbf{v}_l$, and $\mathbf{v}_g$.

To obtain the weak forms, the strong forms of the mixture, liquid phase, and gas phase momentum equations are multiplied by admissible test functions $\delta\mathbf{v}_s$, $\delta\mathbf{v}_l$, and $\delta\mathbf{v}_g$, respectively, and integrated over Ω. This yields

$$\begin{aligned}\int_\Omega \delta\mathbf{v}_s\cdot(1-n)\rho_s\mathbf{a}_s\,d\Omega + \int_\Omega \delta\mathbf{v}_s\cdot nS_l\rho_l\mathbf{a}_l\,d\Omega + \int_\Omega \delta\mathbf{v}_s\cdot nS_g\rho_g\mathbf{a}_g\,d\Omega \\ = -\int_\Omega \boldsymbol{\sigma} : \nabla\delta\mathbf{v}_s\,d\Omega + \int_{\partial\Omega}\delta\mathbf{v}_s\cdot\bar{\mathbf{t}}\,d\Gamma + \int_\Omega \delta\mathbf{v}_s\cdot\rho\mathbf{b}\,d\Omega,\end{aligned} \tag{40}$$

$$\begin{aligned}\int_\Omega \delta\mathbf{v}_l\cdot nS_l\rho_l\mathbf{a}_l\,d\Omega &= \int_\Omega (nS_lP_l)\mathbf{I} : \nabla\delta\mathbf{v}_l\,d\Omega + \int_{\partial\Omega}\delta\mathbf{v}_l\cdot\bar{q}_l\mathbf{n}\,d\Gamma \\ &+ \int_\Omega \delta\mathbf{v}_l\cdot nS_l\rho_l\mathbf{b}\,d\Omega - \int_\Omega \delta\mathbf{v}_l\cdot(nS_l)^2\frac{\mu_l}{k_a k_{rl}}(\mathbf{v}_l-\mathbf{v}_s)\,d\Omega,\end{aligned} \tag{41}$$

$$\begin{aligned}\int_\Omega \delta\mathbf{v}_g\cdot nS_g\rho_g\mathbf{a}_g\,d\Omega &= \int_\Omega (nS_gP_g)\mathbf{I} : \nabla\delta\mathbf{v}_g\,d\Omega + \int_{\partial\Omega}\delta\mathbf{v}_g\cdot\bar{q}_g\mathbf{n}\,d\Gamma \\ &+ \int_\Omega \delta\mathbf{v}_g\cdot nS_g\rho_g\mathbf{b}\,d\Omega - \int_\Omega \delta\mathbf{v}_g\cdot(nS_g)^2\frac{\mu_g}{k_a k_{rg}}(\mathbf{v}_g-\mathbf{v}_s)\,d\Omega,\end{aligned} \tag{42}$$

The domain Ω is discretized into Lagrangian material points embedded in a fixed Eulerian background grid (Yerro et al., 2015; Zhang et al., 2017). Each particle p carries state variables, while the grid nodes i host nodal unknowns. A generic field $f(\mathbf{x})$ is approximated by particle quadrature:

$$\int_\Omega f(\mathbf{x})\,d\Omega \approx \int_\Omega \sum_p f_p\chi_p(\mathbf{x})\,d\Omega, \tag{43}$$

where f_p is the particle value and $\chi_p(\mathbf{x})$ is the particle characteristic function.

Using the nodal shape functions $N_i(\mathbf{x})$, the virtual fields are interpolated as

$$\delta\mathbf{v}_s = \sum_i \delta\mathbf{v}_{si}N_i(\mathbf{x}), \tag{44}$$

$$\delta\mathbf{v}_l = \sum_i \delta\mathbf{v}_{li}N_i(\mathbf{x}), \tag{45}$$

$$\delta\mathbf{v}_g = \sum_i \delta\mathbf{v}_{gi}N_i(\mathbf{x}), \tag{46}$$

In GIMP, each particle is associated with a characteristic function $\chi_p(\mathbf{x})$ that equals 1 inside the particle domain and 0 outside. The particle–grid mapping employs the weighting function S_{ip} and its gradient $\mathbf{G}_{ip}$:

$$S_{ip} = \frac{1}{V_p}\int_{\Omega_p}\chi_p(\mathbf{x})N_i(\mathbf{x})\,d\Omega, \tag{47}$$

$$\mathbf{G}_{ip} = \frac{1}{V_p}\int_{\Omega_p}\chi_p(\mathbf{x})\nabla N_i(\mathbf{x})\,d\Omega, \tag{48}$$

where V_p is the volume of particle p.

Substituting Eqs. (44)–(48) into the weak forms, Eqs. (40)–(42), yields the semi-discrete nodal momentum equations. For the liquid and gas phases, they can be written compactly as

$$\tilde{M}_\alpha\mathbf{a}_\alpha = \mathbf{R}_\alpha^{\mathrm{ext}} + \mathbf{R}_\alpha^{\mathrm{int}} + \Lambda_\alpha^{\mathrm{d}}(\mathbf{v}_\alpha - \mathbf{v}_s), \qquad \alpha = \mathrm{l},\mathrm{g}, \tag{49}$$

where $\tilde{M}_\alpha$ is the lumped nodal mass matrix, $\Lambda_\alpha^{\mathrm{d}}$ is the nodal drag operator, and $\mathbf{R}_\alpha^{\mathrm{ext}}$ and $\mathbf{R}_\alpha^{\mathrm{int}}$ are the external and internal nodal force vectors.

The mixture momentum balance is discretized as

$$\tilde{M}_s\mathbf{a}_s + \tilde{M}_l\mathbf{a}_l + \tilde{M}_g\mathbf{a}_g = \mathbf{R}_{\mathrm{m}}^{\mathrm{ext}} + \mathbf{R}_{\mathrm{m}}^{\mathrm{int}}, \tag{50}$$

with the nodal quantities assembled from particle contributions as

$$\tilde{M}_{\alpha i} = \sum_p V_p n_p S_{\alpha p}\rho_{\alpha p}S_{ip}, \qquad \alpha = \mathrm{l},\mathrm{g}, \tag{51}$$

$$\tilde{M}_{si} = \sum_p V_p(1-n_p)\rho_{sp}S_{ip}, \tag{52}$$

$$\Lambda_{\alpha i}^{\mathrm{d}} = -\sum_p V_p(n_pS_{\alpha p})^2\frac{\mu_{\alpha p}}{k_{\mathrm{a}p}k_{\mathrm{r}\alpha p}}S_{ip}, \qquad \alpha = \mathrm{l},\mathrm{g}, \tag{53}$$

$$\mathbf{R}_{\alpha i}^{\mathrm{ext}} = \sum_p V_p\bar{q}_{\alpha p}\mathbf{n}_pS_{ip} + \sum_p V_pn_pS_{\alpha p}\rho_{\alpha p}\mathbf{b}S_{ip}, \qquad \alpha = \mathrm{l},\mathrm{g}, \tag{54}$$

$$\mathbf{R}_{\alpha i}^{\mathrm{int}} = \sum_p V_pn_pS_{\alpha p}P_{\alpha p}\mathbf{G}_{ip}, \qquad \alpha = \mathrm{l},\mathrm{g}, \tag{55}$$

$$\mathbf{R}_{\mathrm{m}i}^{\mathrm{ext}} = \sum_p V_p\bar{\mathbf{t}}_pS_{ip} + \sum_p V_p\rho_{\mathrm{m}p}\mathbf{b}S_{ip}, \tag{56}$$

$$\mathbf{R}_{\mathrm{m}i}^{\mathrm{int}} = -\sum_p V_p\boldsymbol{\sigma}_p\cdot\mathbf{G}_{ip}, \tag{57}$$

where $\rho_{\mathrm{m}p}$ is the mixture density at particle p.

It is emphasized that the semi-discrete momentum equations are not interpreted here as three uncoupled phase-wise updates. Rather, the coupling is retained through the drag operators, the shared state variables (n, S_α, $k_{\mathrm{r}\alpha}$, and P_α), and the mixture balance. Accordingly, within each explicit time step, the nodal momentum update is performed in a locally coupled manner so that the phase accelerations remain mutually constrained at the nodal level.

4.2. Primary unknowns and explicit staggered time integration

The semi-discrete nodal equations derived in Section 4.1 are advanced in time using an explicit staggered integration scheme. The primary kinematic unknowns are the phase velocities $\mathbf{v}_{\mathrm{s}}$, $\mathbf{v}_{\mathrm{l}}$, and $\mathbf{v}_{\mathrm{g}}$. Although the global update is staggered in time, the nodal momentum update for the three phases is carried out in a locally coupled manner, so that the phase accelerations are solved from a local nodal system that combines the phase momentum equations with the mixture momentum balance, while the interphase drag terms are evaluated from the current nodal velocities.

At each time step t^{n}, the nodal accelerations of the solid skeleton, pore-liquid, and pore-gas are obtained from a local coupled system assembled from the semi-discrete phase-wise and mixture momentum equations. In compact form, the nodal momentum update at an active node i can be written as

$$\mathbf{M}_i^{\mathrm{loc}} \begin{Bmatrix} \mathbf{a}_{si}^{\mathrm{n}} \\ \mathbf{a}_{li}^{\mathrm{n}} \\ \mathbf{a}_{gi}^{\mathrm{n}} \end{Bmatrix} = \begin{Bmatrix} \mathbf{R}_{mi}^{\mathrm{ext}} + \mathbf{R}_{mi}^{\mathrm{int}} \\ \mathbf{R}_{li}^{\mathrm{ext}} + \mathbf{R}_{li}^{\mathrm{int}} + \Lambda_{li}^{\mathrm{d}} \left(\mathbf{v}_{li}^{\mathrm{n}} - \mathbf{v}_{si}^{\mathrm{n}} \right) \\ \mathbf{R}_{gi}^{\mathrm{ext}} + \mathbf{R}_{gi}^{\mathrm{int}} + \Lambda_{gi}^{\mathrm{d}} \left(\mathbf{v}_{gi}^{\mathrm{n}} - \mathbf{v}_{si}^{\mathrm{n}} \right) \end{Bmatrix}, \tag{58}$$

where $\mathbf{M}_i^{\mathrm{loc}}$ is the local nodal coefficient matrix containing the phase masses. The first row represents the mixture momentum balance, while the second and third rows correspond to the liquid and gas momentum equations, respectively. The drag terms are evaluated from the nodal phase velocities at t^n and therefore remain on the right-hand side. The three phase accelerations are obtained from this local nodal system, so that the liquid and gas accelerations and the solid acceleration remain constrained by the mixture momentum balance. This system is solved independently at each active node and yields mutually consistent accelerations for the three phases. In this way, the mixture momentum equation is not used merely as a diagnostic post-processing relation, but contributes directly to the coupled nodal acceleration update.

Once the nodal accelerations are obtained, the nodal velocities are updated explicitly by forward Euler integration:

$$\mathbf{v}_{\pi i}^{\mathrm{n}+1} = \mathbf{v}_{\pi i}^{\mathrm{n}} + \mathbf{a}_{\pi i}^{\mathrm{n}} \Delta t, \qquad \pi = \mathrm{s}, \mathrm{l}, \mathrm{g}, \tag{59}$$

where $\Delta t = t^{\mathrm{n}+1} - t^{\mathrm{n}}$.

To reduce numerical dissipation in the particle velocity update, a FLIP scheme is adopted. For each phase π, the particle velocity is updated using the nodal acceleration increment mapped back to particles:

$$\mathbf{v}_{\pi p}^{\mathrm{n}+1} = \mathbf{v}_{\pi p}^{\mathrm{n}} + \mathbf{A}_{\pi p}^{\mathrm{n}} \Delta t, \qquad \pi = \mathrm{s}, \mathrm{l}, \mathrm{g}, \tag{60}$$

with

$$\mathbf{A}_{\pi p}^{\mathrm{n}} = \sum_i S_{ip}^{\mathrm{n}} \mathbf{a}_{\pi i}^{\mathrm{n}}. \tag{61}$$

Finally, particle positions are updated using a second-order kinematic scheme based on the solid velocity:

$$\mathbf{X}_p^{\mathrm{n}+1} = \mathbf{X}_p^{\mathrm{n}} + \mathbf{v}_{sp}^{\mathrm{n}} \Delta t + \frac{1}{2} \mathbf{A}_{sp}^{\mathrm{n}} \Delta t^2. \tag{62}$$

4.3. Updates of secondary variables

In addition to the phase velocities updated in Section 4.2, several secondary variables are updated at each time step to close the coupled HM system and capture multiphase interactions. These include the effective stress of the solid skeleton, pore-water and pore-gas pressures, porosity, saturation, permeability, and the solid deformation gradient.

The effective stress at particle p is updated using a hypoelastic objective rate with a Jaumann-type correction:

$$\boldsymbol{\sigma}_p'^{\mathrm{n}+1} = \boldsymbol{\sigma}_p'^{\mathrm{n}} + \left(\boldsymbol{\sigma}_p'^{\mathrm{n}} \mathbf{W}_p^{\mathrm{n}} - \mathbf{W}_p^{\mathrm{n}} \boldsymbol{\sigma}_p'^{\mathrm{n}} \right) \Delta t + \mathbb{D} : \left(\dot{\boldsymbol{\varepsilon}}_p^{\mathrm{n}} - \dot{\boldsymbol{\varepsilon}}_p^{p\mathrm{n}} \right) \Delta t, \tag{63}$$

where $\mathbf{W}_p^n$ is the spin tensor of the solid skeleton and $\dot{\boldsymbol{\varepsilon}}_p^n$ is the solid strain-rate tensor. Using the GIMP mapping, these kinematic quantities are evaluated from nodal solid velocities as $\nabla \mathbf{v}_{\mathrm{s}}\big|_p^{\mathrm{n}} = \sum_i \mathbf{v}_{si}^{\mathrm{n}} \otimes \mathbf{G}_{ip}^{\mathrm{n}}$, $\mathbf{W}_p^{\mathrm{n}} = \frac{1}{2} \left[\nabla \mathbf{v}_{\mathrm{s}}\big|_p^{\mathrm{n}} - \left(\nabla \mathbf{v}_{\mathrm{s}}\big|_p^{\mathrm{n}} \right)^T \right]$, $\dot{\boldsymbol{\varepsilon}}_p^{\mathrm{n}} = \frac{1}{2} \left[\nabla \mathbf{v}_{\mathrm{s}}\big|_p^{\mathrm{n}} + \left(\nabla \mathbf{v}_{\mathrm{s}}\big|_p^{\mathrm{n}} \right)^T \right]$.

Pore-water and pore-gas pressures are updated from the pressure evolution equations, Eqs. (10)–(11). At each particle p, the pressure rates $\dot{P}_{lp}^{\mathrm{n}}$ and $\dot{P}_{gp}^{\mathrm{n}}$ are obtained by solving a 2×2 linear system:

$$A_{\mathrm{ll}} \dot{P}_{\mathrm{l}}^{\mathrm{n}} + B_{\mathrm{lg}} \dot{P}_{\mathrm{g}}^{\mathrm{n}} = X_{\mathrm{l}}, \tag{64}$$

$$A_{\mathrm{gg}} \dot{P}_{\mathrm{g}}^{\mathrm{n}} + B_{\mathrm{lg}} \dot{P}_{\mathrm{l}}^{\mathrm{n}} = X_{\mathrm{g}}. \tag{65}$$

For the isothermal HM setting adopted in this work, the coefficients are written as

$$A_{\mathrm{ll}} = n \left(\frac{S_{\mathrm{l}}}{K_{\mathrm{l}}} + \frac{\partial S_{\mathrm{l}}}{\partial P_{\mathrm{l}}} \right), \tag{66}$$

$$A_{\mathrm{gg}} = n \left(\frac{S_{\mathrm{g}} M_{\mathrm{g}}}{\rho_{\mathrm{g}} RT} + \frac{\partial S_{\mathrm{l}}}{\partial P_{\mathrm{l}}} \right), \tag{67}$$

$$B_{\mathrm{lg}} = -n \frac{\partial S_{\mathrm{l}}}{\partial P_{\mathrm{l}}}, \tag{68}$$

and the source terms are

$$X_{\mathrm{l}} = -S_{\mathrm{l}} \dot{\varepsilon}_{\mathrm{s}}^{\mathrm{v}} - n S_{\mathrm{l}} \left(\dot{\varepsilon}_{\mathrm{l}}^{\mathrm{v}} - \dot{\varepsilon}_{\mathrm{s}}^{\mathrm{v}} \right), \tag{69}$$

$$X_{\mathrm{g}} = -S_{\mathrm{g}} \dot{\varepsilon}_{\mathrm{s}}^{\mathrm{v}} - n S_{\mathrm{g}} \left(\dot{\varepsilon}_{\mathrm{g}}^{\mathrm{v}} - \dot{\varepsilon}_{\mathrm{s}}^{\mathrm{v}} \right), \tag{70}$$

where $\dot{\varepsilon}_\pi^{\mathrm{v}} = \nabla \cdot \mathbf{v}_\pi$ is the volumetric strain rate of phase π ($\pi = \mathrm{s}, \mathrm{l}, \mathrm{g}$), evaluated at particle p. The phase volumetric strain rates are computed from the corresponding velocity gradients obtained via GIMP mapping: $\nabla \mathbf{v}_\pi\big|_p^{\mathrm{n}} = \sum_i \mathbf{v}_{\pi i}^{\mathrm{n}} \otimes \mathbf{G}_{ip}^{\mathrm{n}}$, $\dot{\boldsymbol{\varepsilon}}_\pi = \frac{1}{2} \left[\nabla \mathbf{v}_\pi + \left(\nabla \mathbf{v}_\pi \right)^T \right]$, $\dot{\varepsilon}_\pi^{\mathrm{v}} = \mathrm{tr}\left(\dot{\boldsymbol{\varepsilon}}_\pi \right)$.

In matrix form,

$$\begin{bmatrix} A_{\mathrm{ll}} & B_{\mathrm{lg}} \\ B_{\mathrm{lg}} & A_{\mathrm{gg}} \end{bmatrix} \begin{Bmatrix} \dot{P}_{lp}^{\mathrm{n}} \\ \dot{P}_{gp}^{\mathrm{n}} \end{Bmatrix} = \begin{Bmatrix} X_{\mathrm{l}} \\ X_{\mathrm{g}} \end{Bmatrix}, \tag{71}$$

and the pressures are updated by forward Euler integration:

$$P_{\alpha p}^{\mathrm{n}+1} = P_{\alpha p}^{\mathrm{n}} + \dot{P}_{\alpha p}^{\mathrm{n}} \Delta t, \qquad \alpha = \mathrm{l}, \mathrm{g}, \tag{72}$$

The solid deformation gradient at particle p is updated multiplicatively as $\mathbf{F}_{sp}^{\mathrm{n}+1} = d\mathbf{F}_{sp}^{\mathrm{n}+1} \mathbf{F}_{sp}^{\mathrm{n}}$, where the incremental deformation gradient is given by $d\mathbf{F}_{sp}^{\mathrm{n}+1} = \mathbf{I} + \Delta t \sum_i \mathbf{v}_{si}^{\mathrm{n}} \otimes \mathbf{G}_{ip}^{\mathrm{n}}$. The updated Jacobian of the solid-phase transformation, $J_p^{\mathrm{n}+1} = \det\left(\mathbf{F}_{sp}^{\mathrm{n}+1} \right)$, is then used to update the particle volume and porosity:

$$V_p^{\mathrm{n}+1} = J_p^{\mathrm{n}+1} V_p^0, \tag{73}$$

$$n_p^{\mathrm{n}+1} = 1 - \frac{1 - n_p^0}{J_p^{\mathrm{n}+1}}, \tag{74}$$

where V_p^0 is the initial particle volume.

Finally, the phase densities are updated using Eqs. (5) and (6), saturation is evaluated from Eqs. (35)–(36), relative permeabilities from Eqs. (37)–(38), and the intrinsic permeability from Eq. (39).

4.4. Solution algorithm and numerical stability

Fig. 2 summarizes the explicit GIMP solution procedure adopted for the coupled three-phase HM formulation, as implemented in the CB-Geo MPM framework. At $t = 0$, the particle state variables $\{\rho_{\pi p}^0, \mathbf{v}_{\pi p}^0, P_{\alpha p}^0, S_{\alpha p}^0, S_{\mathrm{r}\alpha p}^0, k_{\alpha p}^0, k_{\mathrm{r}\alpha p}^0, n_p^0, V_p^0\}$ are prescribed, with $\pi = \mathrm{s, l, g}$ and $\alpha = \mathrm{l, g}$. The solution is then advanced in time by repeating the following steps over each increment $t^{\mathrm{n}} \to t^{\mathrm{n+1}}$.

Step 0: Initialization. Initialize the background grid and evaluate the GIMP shape functions S_{ip} and their gradients $\mathbf{G}_{ip}$ for all active particles.

Step 1: Particle-to-grid transfer (P2G). Project the particle phase velocities $\mathbf{v}_{\pi p}^{\mathrm{n}}$ to the background grid to obtain the nodal phase velocities $\mathbf{v}_{\pi i}^{\mathrm{n}}$. These nodal velocity fields provide the kinematic information required for the subsequent stress and pressure updates.

Step 2: Stress update. Compute the particle strain-rate measures from the nodal velocity gradients using Eq. (29). When plastic yielding is activated, the plastic strain increment is evaluated using Eq. (30). The effective stress $\boldsymbol{\sigma}_p'^{\mathrm{n+1}}$ is then updated through the objective hypoelastic integration with Jaumann correction, Eq. (63).

Step 3: Update hydraulic state variables. Update the phase densities using the compressibility relations, Eqs. (5)–(6). The liquid saturation is then updated from the SWRC, Eqs. (35)–(36), followed by the evaluation of the relative permeabilities from Eqs. (37)–(38) and the intrinsic permeability from Eq. (39). The solid deformation gradient and its Jacobian are subsequently updated, after which the particle volume and porosity are updated via Eqs. (73)–(74).

Step 4: Explicit staggered pressure predictor. Update the pore-water and pore-gas pressures, $\{P_{\mathrm{l}p}^{\mathrm{n+1}}, P_{\mathrm{g}p}^{\mathrm{n+1}}\}$, by solving the coupled 2×2 system, Eqs. (64)–(71), and then advancing the pressures using the forward-Euler update, Eq. (72). This staggered predictor is performed before assembling the nodal forces, so that the updated pore pressures are consistently incorporated into the evaluation of internal forces.

Step 5: Assembly of nodal equations. Assemble the lumped nodal masses $\tilde{M}_{\alpha i}$ and $\tilde{M}_{si}$, the drag operators $\Lambda_{\alpha i}^{\mathrm{d}}$, and the external and internal nodal force vectors $\mathbf{R}_{\alpha i}$ and $\mathbf{R}_{\mathrm{m}i}$ from particle contributions using Eqs. (51)–(57).

Step 6: Coupled nodal momentum solve and explicit velocity update. Assemble and solve the local coupled nodal momentum system, Eq. (58), to obtain the nodal accelerations of the solid, liquid, and gas phases. The nodal phase velocities are then advanced explicitly over Δt using Eq. (59).

Step 7: Grid-to-particle transfer (G2P) and advection. Map the nodal accelerations back to the particles and update the particle phase velocities $\mathbf{v}_{\pi p}^{\mathrm{n+1}}$ using the FLIP-style update, Eqs. (60)–(61). The particle positions $\mathbf{x}_p^{\mathrm{n+1}}$ are then advanced using the second-order kinematic update in Eq. (62).

The above procedure is repeated until $t^{\mathrm{n}} \geq t_{\mathrm{final}}$. The time step Δt is chosen to satisfy the stability requirements of the explicit integration, including the mechanical CFL constraint and the additional stiffness associated with interphase drag coupling.

To maintain numerical stability of the explicit staggered HM-MPM formulation, the admissible time step must remain sufficiently small with respect to both inertial wave propagation and drag-induced stiffness. For explicit MPM, a standard reference estimate is the mechanical CFL condition, $\Delta t_{\mathrm{CFL}} \sim h/c$, where h is the minimum grid spacing and c is a characteristic wave speed. In the present three-phase formulation, an additional restriction arises from the drag-induced coupling in the local nodal momentum system. A convenient estimate is therefore

$$\Delta t \leq \min\left(\Delta t_{\mathrm{CFL}}, \Delta t_{\mathrm{drag,l}}, \Delta t_{\mathrm{drag,g}}\right), \tag{75}$$

with

$$\Delta t_{\mathrm{drag},\alpha} \sim \frac{\tilde{M}_\alpha}{|\Lambda_\alpha^{\mathrm{d}}|}, \qquad \alpha = \mathrm{l, g}, \tag{76}$$

where $\tilde{M}_\alpha$ and $\Lambda_\alpha^{\mathrm{d}}$ denote the nodal phase mass and drag operator, respectively. These estimates show that the admissible time step decreases not only with increasing wave speed but also with stronger interphase drag, such as under lower permeability or higher fluid viscosity. In all simulations presented here, Δt was selected conservatively below the most restrictive coupled stability bound and was verified numerically to produce stable benchmark responses without spurious oscillations.

5. Benchmark examples and validation

5.1. 1D saturated consolidation

To verify the spatial discretization and explicit time integration of the proposed MPM framework, the classical one-dimensional (1D) saturated consolidation problem is first reproduced using the analytical Terzaghi solution as reference. A saturated soil column of height $H = 1$ m is considered (Fig. 3). The bottom boundary is fixed ($u = 0$), and the lateral boundaries are rollers, allowing vertical deformation while preventing lateral displacement. A constant surface surcharge q_{s} is applied at the top. For the hydraulic condition, the top boundary is drained, whereas the bottom boundary is impermeable. The solid skeleton is modelled as linear elastic under small strain, and pore-water flow follows Darcy's law. Unless otherwise stated, the material and transport parameters are $\rho_{\mathrm{s}} = 2650$ kg/m^3, $\rho_{\mathrm{l}} = 1000$ kg/m^3, $n = 0.4$, $E = 10$ MPa, $\nu = 0.0$, $\mu_{\mathrm{l}} = 1 \times 10^{-3}$ Pa s, $k_{\mathrm{a}} = 1.03 \times 10^{-10}$ m^2, and $K_{\mathrm{l}} = 2 \times 10^9$ Pa. The column is discretized into 50 uniform cells ($\Delta z = 0.02$ m), and explicit time integration is performed with $\Delta t = 1 \times 10^{-5}$ s.

The excess pore-water pressure $p(z, t)$ in Terzaghi's 1D consolidation is given by (Terzaghi, 1943),

$$p(z,t) = \sum_{n=0}^{\infty} \frac{2}{\xi H} \sin(\xi z) e^{-\xi^2 c_v t}, \qquad \xi = \frac{(2n+1)\pi}{2H}, \tag{77}$$

where $z \in [0, H]$ is the vertical coordinate measured from the drained boundary, and c_v is the consolidation coefficient. The surface settlement $u_{\mathrm{s}}(t)$ follows from 1D compression under effective stress and can be written as

$$u_{\mathrm{s}}(t) = \frac{H}{M}\left\{ q_{\mathrm{s}} - \sum_{n=0}^{\infty} \frac{2}{\xi^2 H^2} e^{-\xi^2 c_v t} \right\}, \tag{78}$$

where M is the constrained modulus of the skeleton. These expressions serve as the reference solution for verification.

Fig. 4(a) compares the computed surface settlement history with the analytical Terzaghi consolidation solution. The proposed MPM prediction closely follows the analytical curve over the entire time range on the logarithmic time axis. The settlement increases rapidly at early time, reflecting the initial generation of excess pore pressure under the applied surcharge, and then gradually approaches a stable value as pore pressure dissipates and effective stress is transferred to the skeleton. The agreement indicates that the explicit GIMP–MPM scheme captures both the transient consolidation rate and the final settlement without spurious numerical oscillations.

Fig. 4(b) compares the excess pore-water pressure distributions along the column depth predicted by the proposed MPM scheme with the analytical Terzaghi solution at $t = 0.04$, 0.1, 0.2, 0.5, 1.5, and 2.5 s. At early times ($t = 0.04$–0.2 s), the pressure profiles exhibit pronounced gradients, indicating rapid drainage near the drained boundary and a delayed response in the deeper zone. As time increases ($t \geq 1.0$ s), the profiles progressively contract towards zero excess pressure and become increasingly uniform, reflecting diffusion-dominated dissipation and the gradual transfer of load from pore pressure to skeleton effective stress. Across all time snapshots, the MPM curves closely match the analytical solution, confirming accurate spatial discretization of the consolidation-diffusion process and stable explicit integration without spurious oscillations.

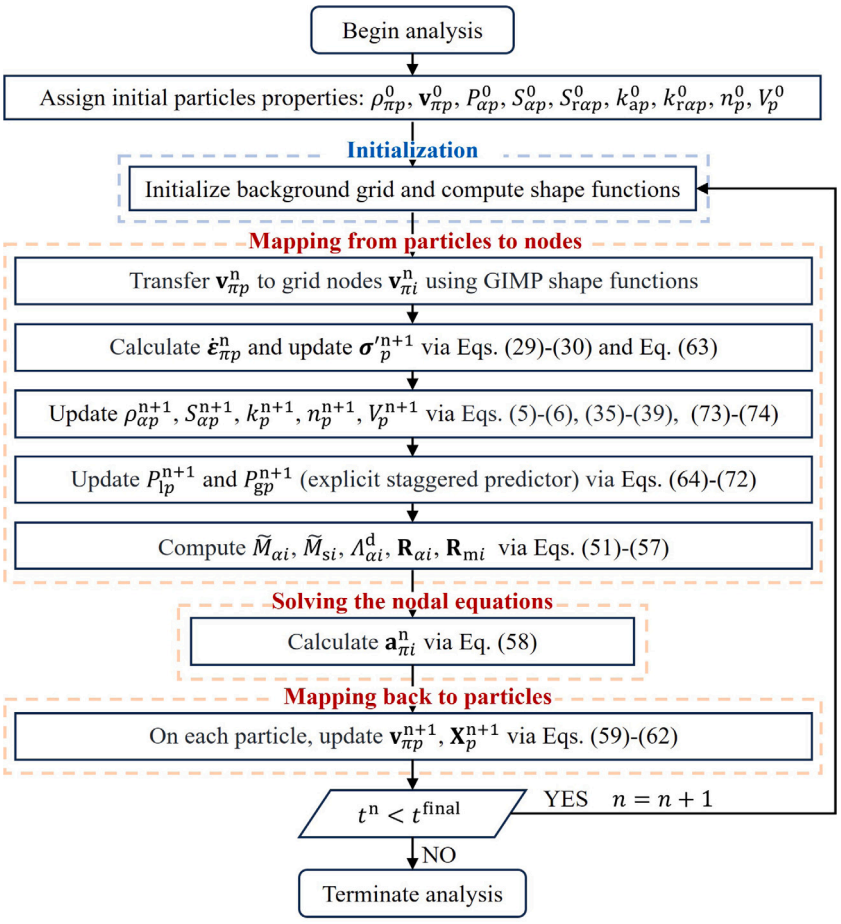


Fig. 2. Flowchart of the explicit staggered three-phase GIMP-MPM algorithm, showing particle–grid transfers, pore-pressure predictor, nodal momentum solves, and particle updates for coupled HM simulations.

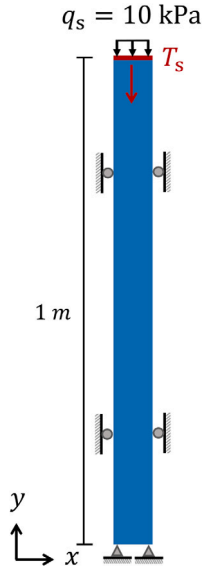


Fig. 3. Geometry and boundary conditions for a saturated column, with the top subjected to constant surface surcharge.

5.2. 1D consolidation of unsaturated porous column

We validate the proposed three-phase MPM against the isothermal unsaturated column benchmark of Yu et al. (2025), while adopting several material constants consistent with Lei et al. (2021) for ease of comparison. The benchmark considers a 1D porous column of height $H = 1$ m, with the same geometry as Fig. 3. The initial state is prescribed by a linear soil water retention curve (SWRC), $P_c = 10^6(1 - S_l)$ Pa, giving the homogeneous matric suction $P_c = 300$ kPa and liquid saturation $S_l = 0.7$. At $t = 0^+$, the top boundary is subjected to a suction step: $P_c = 300$ kPa changes to $P_c = 500$ kPa. The bottom is kinematically fixed in the vertical direction, and lateral boundaries are rollers. Liquid is undrained at the bottom, while the surface gas pressure is vented and fixed at $P_g = 100$ kPa (drainage). For this benchmark only, pressures are reported in the absolute convention adopted by Yu et al. (2025), so that atmospheric pore-gas pressure is 100 kPa. All subsequent slope results are reported as gauge pressures unless otherwise stated. The interior gas pressure evolves spatiotemporally as part of the three-phase formulation. All simulations are isothermal. The material properties are given as follows: $\rho_s = 2500$ kg/m^3, $\rho_l = 1000$ kg/m^3, $M_g = 0.029$ kg/mol, $n = 0.3$, $K_l = 2 \times 10^9$ Pa, $E = 10$ MPa, $\nu = 0.4$, $\mu_l = 1 \times 10^{-3}$ Pa s, $\mu_g = 1\times10^{-5}$ Pa s, $k_{al} = k_{ag} = 5\times10^{-11}$ m^2. The column is discretized into 50 uniform 1D elements ($\Delta z = 0.02$ m), and explicit time integration is used with $\Delta t = 1 \times 10^{-5}$ s.

To isolate the impact of saturation-dependent mobility, two relative permeability options are considered for the three-phase model. The baseline assumes constant mobilities, $k_{rl} = k_{rg} = 1$; the alternative adopts the Brooks–Corey relations

$$k_{rl} = S_e^{3+2m_p}, \tag{79}$$

$$k_{rg} = (1 - S_e)^2(1 - S_e^{3+2m_p}), \tag{80}$$

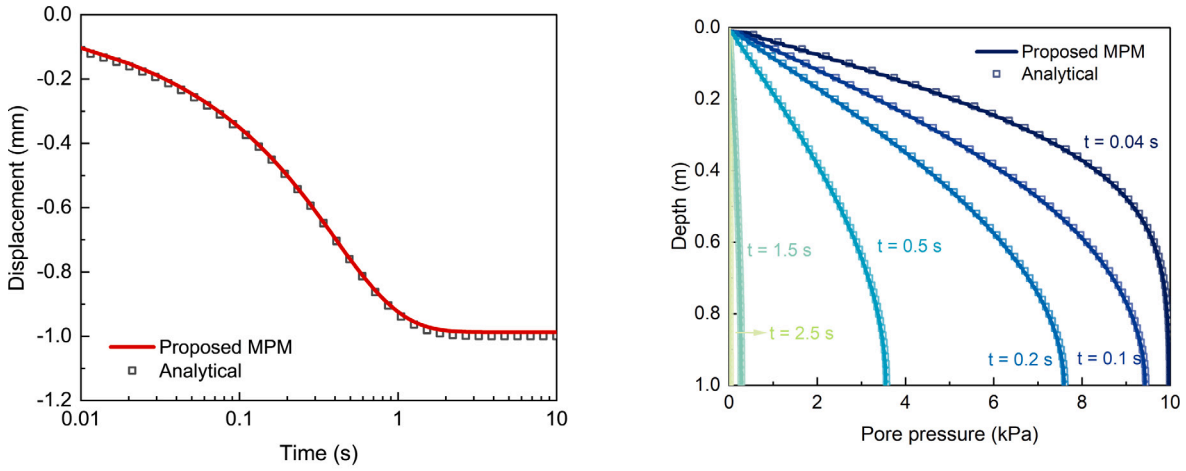


Fig. 4. 1D saturated consolidation benchmark: (a) surface settlement history, comparing the proposed MPM prediction with the analytical Terzaghi solution; (b) excess pore-water pressure profiles along the column depth at representative times.

where $S_e = (S_l - S_{lc})/(1 - S_{lc})$ is the effective degree of saturation, $S_{lc} = 0$ is the irreducible water saturation, and $m_p = 0.3$ is the pore size distribution index, respectively, in this example. The quantities of interest are the time histories at the column base of suction P_c, pore-gas pressure P_g, and pore-liquid pressure P_l, together with the surface displacement u_s.

Base-point histories on a logarithmic time axis (Fig. 5) show that the suction rises from 300 to 500 kPa, with the same onset and inflection times as reported by Yu et al. (2025) (Fig. 5(a)). For the gas phase, introducing Brooks–Corey permeabilities produces the characteristic transient under-pressure before recovery to 100 kPa; the depth and timing of this dip coincide with the reference (Fig. 5(b)). The liquid pressure dissipates smoothly, and its rapid decay phase aligns with the recovery of P_g, evidencing the expected gas–liquid coupling (Fig. 5(c)). The surface settlement increases monotonically towards a common final value (Fig. 5(d)). Saturation-dependent permeabilities cause a modest early–mid-time delay relative to constant mobility, consistent with Yu's trends. Small early-time ripples due to explicit stepping under a step load remain bounded and do not affect the steady states.

Depth-wise snapshots (Fig. 6) confirm spatial consistency. The advancing suction/saturation front is captured at the correct depth and slope at all reported times; porosity changes are small (order 10^{-3}) and systematic; displacement profiles are smooth and monotone. Front positions and thicknesses agree with Yu et al. (2025) across snapshots. Overall, the temporal and spatial agreements, covering suction, gas and liquid pressures, saturation, porosity, and settlement, validate the accuracy and robustness of the three-phase MPM with either constant or Brooks–Corey relative permeability. No spurious oscillations are observed in this benchmark, and the selected discretization reproduces the reference histories over the reported interval.

5.3. Experimental validation of vented and confined column infiltration

The gas phase implementation was further validated against the paired transparent column experiments of Siemens et al. (2013). These tests provide direct measurements of wetting front advance and pore-air pressure under contrasting gas boundary conditions, complementing the benchmarks presented above.

The experimental apparatus is shown in Fig. 7(a). It consisted of a 1.45 m high transparent column containing a 1.075 m packed specimen of coarse fused quartz. The internal cross section was 45.6 mm × 45.6 mm. Six pore pressure transducers measured pore-air pressure before arrival of the wetting front and pore-oil pressure after the front had passed. Wetting front positions were obtained independently from image analysis. Two boundary conditions were considered. In the vented test, constant liquid heads were maintained at the top and bottom, while lateral instrumentation ports allowed pore-air to escape. Pore-air pressure therefore remained close to atmospheric pressure. In the confined test, oil was supplied from the top under the same constant head, but the base was impermeable, and the lateral ports were closed. The advancing wetting front consequently compressed the gas ahead of it. The applied oil head was approximately 120 mm, equivalent to 995 Pa.

The numerical column was represented by a two-dimensional (2D) strip one cell in width. The cell size was 11.4 mm, and four material points were assigned to each cell, giving 376 particles in total. The fused-quartz skeleton was treated as rigid because deformation was negligible in the experiment. The porosity was 0.50, while the oil density and dynamic viscosity were $845\,\mathrm{kg/m^3}$ and $0.0101\,\mathrm{Pa\,s}$, respectively. The intrinsic permeability was $1.8282 \times 10^{-9}\,\mathrm{m^2}$. The measured residual saturation, retention exponent, and saturation behind the wetting front were adopted from the experiments. Pressure was integrated semi-implicitly over the complete 875 s test period. Gravity was omitted to isolate the capillary and pore-gas mechanisms that distinguish the two boundary conditions.

The numerical wetting front was defined as the deepest layer with $S_l \geq 0.40$ that remained continuously connected to the loaded surface. Experimental front positions were digitized from Siemens et al. (2013). Fig. 7(b) shows that the model captures the rapid front advance under vented conditions and the marked retardation caused by confined gas. The differences between the simulated and digitized front positions are generally of the order of 10–20 mm, comparable with one to two vertical grid intervals. A larger discrepancy appears near the end of the confined test, where the numerical front reaches the deepest resolved position approximately 100 s earlier than observed.

The pore-air pressure provides a direct test of the gas response. Under vented conditions, the computed pressure ahead of the front remains atmospheric, consistent with the measurements. Under confined conditions, the model reproduces the rapid pressure increase during the first 25 s, with differences generally of the order of 0.1 kPa from the digitized values in Fig. 7(c). The pressure then stabilizes near 1.4 kPa, within the reported experimental range of 1.2–1.6 kPa, as shown in Fig. 7(d). A virtual transducer is included in the dry-zone average only while its location remains ahead of the wetting front. These results support the model's ability to reproduce gas compression and hydraulic retardation under the tested boundary conditions.

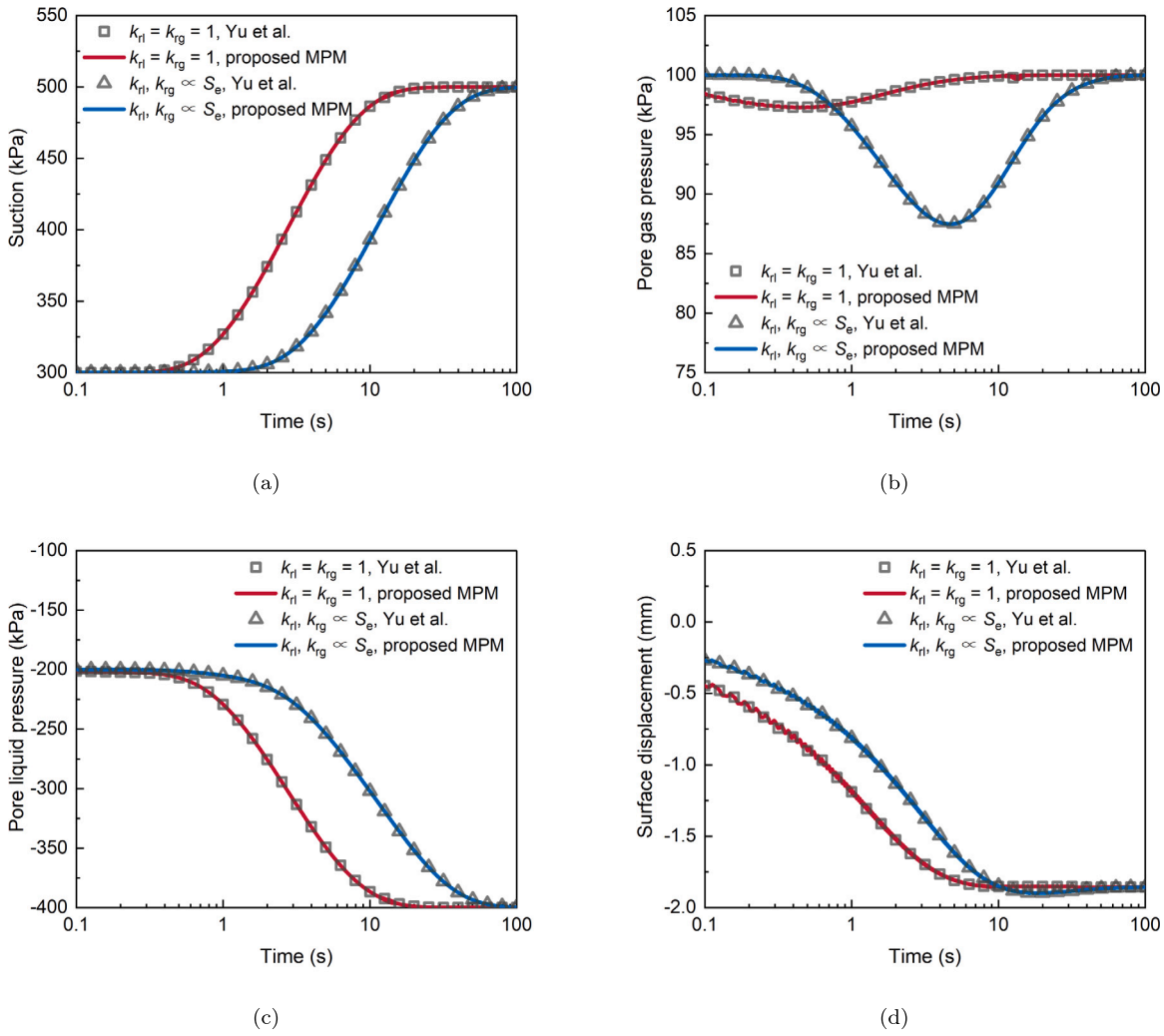


Fig. 5. Evolution of (a) suction P_c, (b) pore-gas pressure P_g, (c) pore-liquid pressure P_l at the column base, and (d) surface displacement u_s, predicted by the three-phase MPM. red: constant $k_{rl}, k_{rg} = 1$; blue: Brooks–Corey $k_r(S_e)$. (For interpretation of the references to colour in this figure legend, the reader is referred to the web version of this article.)

5.4. Large deformation wetting-induced slope benchmark

To further assess the capability of the proposed three-phase HM–MPM framework in a large deformation setting, an additional benchmark comparison is conducted using the unsaturated slope wetting and failure study reported by Di Carluccio et al. (2025). In that work, an MPM model was used to reproduce a centrifuge experiment involving wetting, failure initiation, large post-failure deformation, and final deposition of an unsaturated slope. The reference study presented the slope geometry, boundary conditions, staged construction procedure, and wetting scenario, and then compared the numerical predictions with experimental images in terms of wetting-front evolution and deformation pattern. In addition to the experimental images, the reference study also reported corresponding MPM results, including the deformed slope profile and the interpreted wetting-front position. It therefore provides a useful large deformation reference beyond the 1D verification cases considered above.

In the reference study by Di Carluccio et al. (2025), the physical model consists of a silty clay slope constructed in a transparent centrifuge box and subsequently wetted from the base. The model slope is approximately 0.15 m high and 0.27 m wide, with an initial inclination of about 50°. A gravel column is placed adjacent to the right side of the slope to control the water level and promote wetting from the lower boundary. Their numerical model reproduces this geometry, applies fixed mechanical boundaries at the base, allows seepage at the free surface, and imposes wetting by increasing pore-water pressure at the base near the gravel column. The complete experimental configuration, scaling conditions, construction procedure, and measurement details are reported by Di Carluccio et al. (2025). The present section summarizes only the information required to define and interpret the numerical validation.

In the present comparison, the same overall slope geometry, loading scenario, and reference material setting are adopted from Di Carluccio et al. (2025). The computational grid uses a cell size of 0.01 m, and the material points are initialized with a particle size of 0.005 m, giving a total of 931 particles in the slope domain. In addition, because the present simulations are carried out using an explicit MPM formulation, a smaller time step of $\Delta t = 10^{-5}$ s is used to maintain numerical stability. The purpose of this benchmark is not to reproduce the full constitutive calibration procedure of Di Carluccio et al. (2025), but rather to examine whether the present three-phase formulation can capture the main coupled wetting–deformation features of a large deformation unsaturated slope problem.

Fig. 8 compares three representative stages of slope evolution. In the reference study, these stages correspond to the experimental images reported at 22 s, 62 s, and 122 s during the wetting and failure process. Figs. 8(a)–8(c) show the experimental images reported by Di Carluccio et al. (2025), in which the interpreted wetting front is indicated by

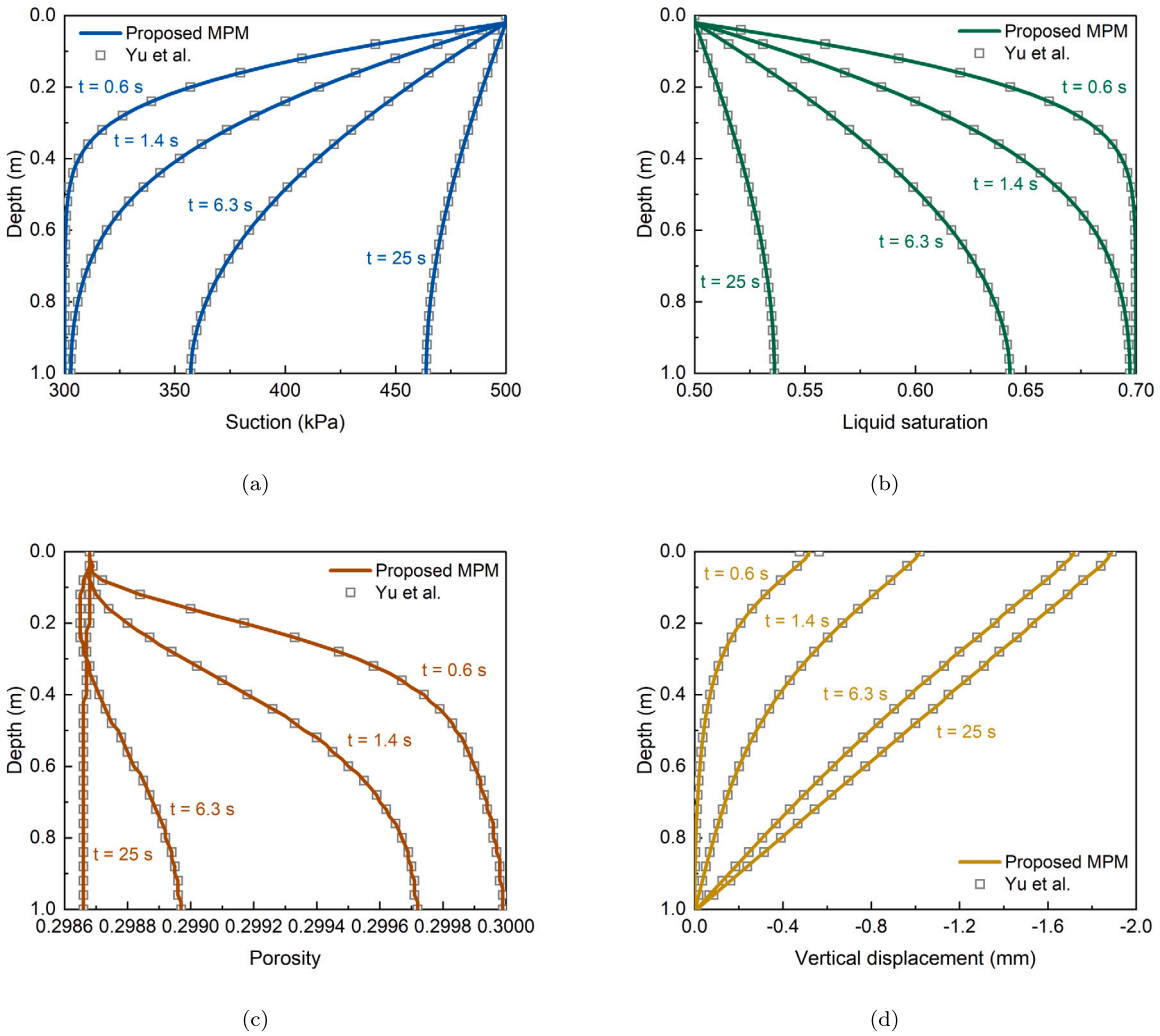


Fig. 6. Depth-wise profiles of (a) suction $P_c(z)$, (b) liquid saturation $S_l(z)$, (c) porosity $n(z)$, and (d) vertical displacement $u(z)$ at $t = 0.6$, 1.4, 6.3, and 25 s.

the dashed blue line. Figs. 8(d)–8(f) show the corresponding results from the present three-phase HM–MPM simulation in terms of liquid saturation and deformed slope profile. For ease of comparison, the deformed profile and the $S_l = 0.99$ contour reported by Di Carluccio et al. (2025) from their MPM simulation are also superimposed in Figs. 8(d)–8(f). The comparison shows that the present model reproduces the main trend of wetting-front propagation from the toe region towards the interior of the slope, together with the progressive development of slope deformation and the overall change in slope profile.

At the early stage, the predicted high saturation zone remains localized near the toe, and the deformed slope profile stays close to the initial geometry, consistent with the experimental image in Fig. 8(a) and the corresponding numerical comparison in Fig. 8(d). At the intermediate stage, the wetting front advances upward and inward, while the crest begins to settle and the slope profile starts to deviate noticeably from the initial configuration. The present simulation captures this transition and shows good qualitative agreement with both the experimental image in Fig. 8(b) and the corresponding numerical comparison in Fig. 8(e). At the later stage, the slope undergoes a clear large deformation and enters the failure regime. As shown in Figs. 8(c) and 8(f), the present model reproduces the overall failure morphology and the main shape of the deformed profile, while the predicted $S_l = 0.99$ contour follows the same general trend as that reported by Di Carluccio et al. (2025).

Some discrepancies remain, especially in the exact position of the $S_l = 0.99$ contour and in the final local surface shape. These differences are expected because the present study uses a different HM formulation and does not attempt to reproduce the full constitutive calibration procedure adopted in the reference work. Nevertheless, the comparison provides an important intermediate benchmark between the 1D verification problems and the demonstrative slope analyses presented in the next section. In particular, it indicates that the present three-phase HM–MPM framework is able to reproduce the main wetting-front evolution and large-deformation failure morphology of an unsaturated slope under wetting, which supports its use for the mechanism-oriented analyses developed later.

6. Modelling slope failure during rapid hydraulic loading: the role of evolving pore-gas pressure

This section examines how evolving pore-gas pressure affects wetting, stress redistribution, and failure onset in a partially saturated slope subjected to rapid surface hydraulic loading. An idealized 2D model is used to isolate the gas response as the loading increases from infiltration without ponding to severe surface inundation. The analysis first establishes the weak loading response, then identifies the transition to active gas control, and finally explains why earlier failure can occur despite a shallower wetting front.

6.1. Slope model setup and loading conditions

The model represents a generic homogeneous earth embankment or engineered soil slope rather than a reconstruction of a specific

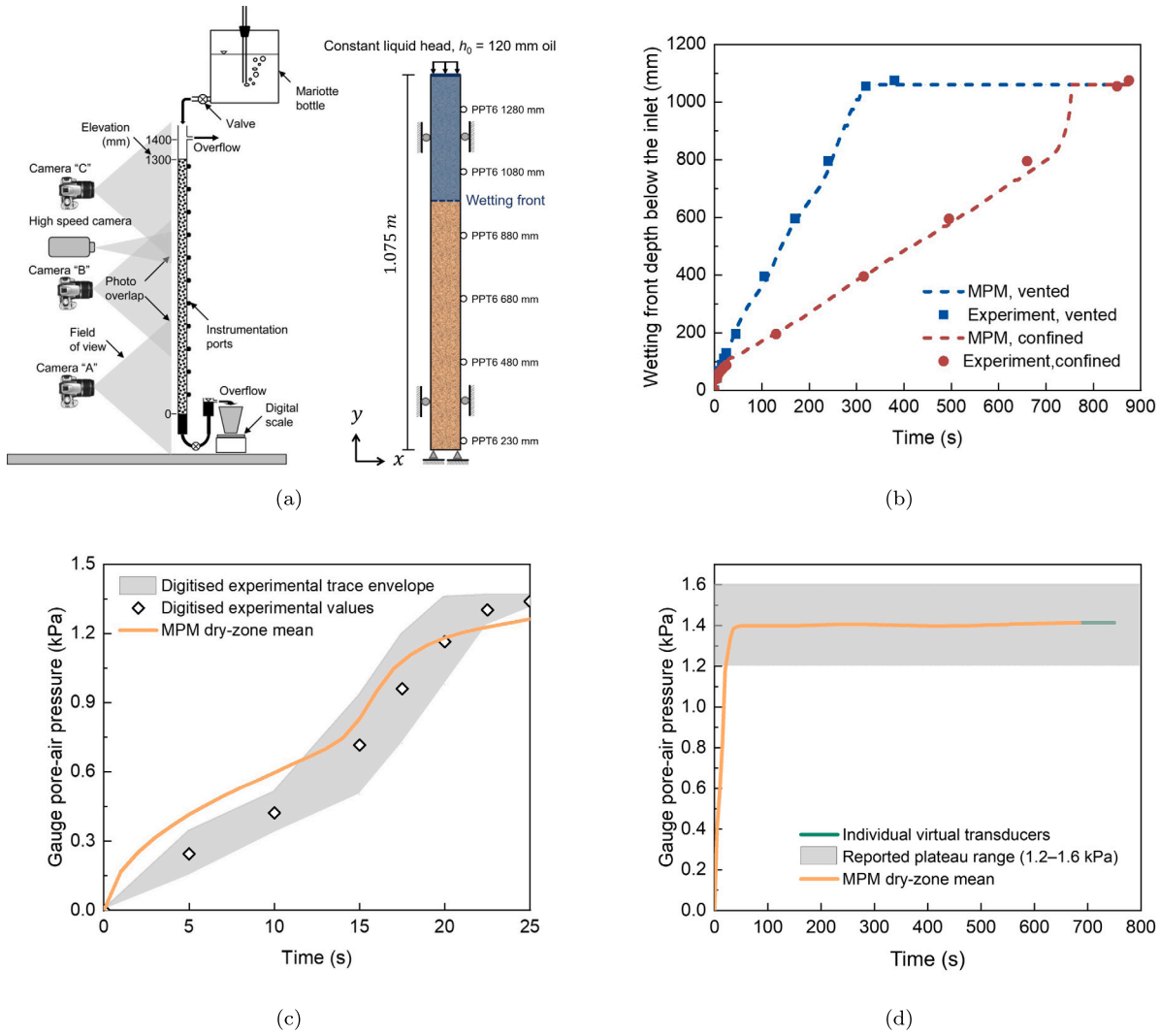


Fig. 7. Validation against the column tests of Siemens et al. (2013): (a) experimental setup and transducer locations, reproduced from Siemens et al. (2013); (b) wetting-front advance under vented and confined conditions; (c) initial confined pore-air pressure; (d) confined pressure history. The grey region in (c) represents the digitized range of the published traces. Virtual transducers are included only while located ahead of the wetting front.

field site. The slope is treated as a single partially saturated soil layer resting on a rigid and impermeable foundation. No internal drainage layer, weak interlayer, pre-existing slip surface, or spatial variation in material properties is introduced. Before hydraulic loading, the slope remains unsaturated and contains no elevated internal phreatic surface. This simplified engineering geological setting is selected to isolate the coupled response of the soil skeleton, pore-water and pore-gas under rapid surface loading.

The slope is represented by Lagrangian material points moving through a fixed Eulerian background grid. The hydraulically loaded ground surface is treated using prescribed pressure conditions. In the baseline case without ponding, the pore-gas pressure at exposed surface particles is maintained at the atmospheric reference value, while pore-water pressure is prescribed through an equivalent water head. The modified condition used for elevated surface heads is described in Section 6.4. In all cases, water entry is driven by the imposed pressure difference rather than by a prescribed inflow rate. This treatment is consistent with common representations of unsaturated infiltration based on prescribed head, prescribed flux, or atmospheric boundary conditions (Tracy and Vahedifard, 2022; Weill et al., 2009). The bottom boundary is mechanically fixed and impermeable to both fluid phases. The lateral boundaries are constrained horizontally to prevent rigid body motion, but remain hydraulically open so that water and gas can leave the domain. This arrangement limits artificial pressure accumulation at the sides while retaining restricted venting across the hydraulically loaded surface.

The initial condition shown in Fig. 9 is established before the application of any external water head. The material points are initialized with liquid and gas saturations of $S_l^0 = 0.4$ and $S_g^0 = 0.6$, respectively. From the SWRC in Eqs. (35)–(36), together with the parameters in Table 1, this state corresponds to an initial matric suction of approximately 821 kPa. With an initial gas gauge pressure of $P_g^0 = 0$, the corresponding liquid pressure is $P_l^0 \approx -821$ kPa. The listed saturation values therefore refer to the state before gravity equilibration and are fully consistent with the adopted SWRC. Starting from this state, the coupled solid, liquid, and gas system is allowed to equilibrate under self-weight until the velocity, stress, and pressure fields become stable. The subsequent differences between simulations can therefore be attributed to the imposed hydraulic loading rather than to initialization transients.

A single crest displacement criterion is used to define failure onset in the main slope analyses. The material point at the upper end of the inclined slope surface is tracked from the gravity-equilibrated configuration. The failure onset time, t_f, is defined as the first time at which its downward vertical displacement reaches 0.2 m: $t_f = \min\left\{t : -u_y^{crest}(t) \geq 0.2\ \text{m}\right\}$. The same monitoring point and threshold

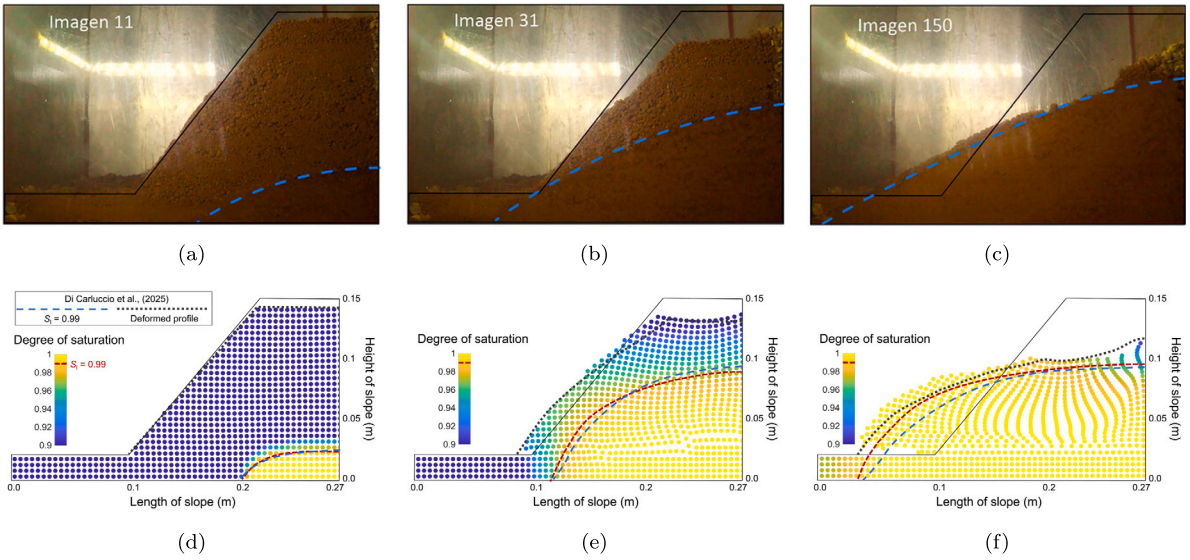


Fig. 8. Large-deformation wetting-induced slope benchmark at three representative stages: (a)–(c) experimental images from Di Carluccio et al. (2025), corresponding to 22 s, 62 s, and 122 s, respectively; (d)–(f) corresponding HM-MPM predictions of liquid saturation and deformed slope profile. The S_l = 0.99 contour and deformed profile reported by Di Carluccio et al. (2025), obtained from their MPM simulation, are included in (d)–(f) for comparison.

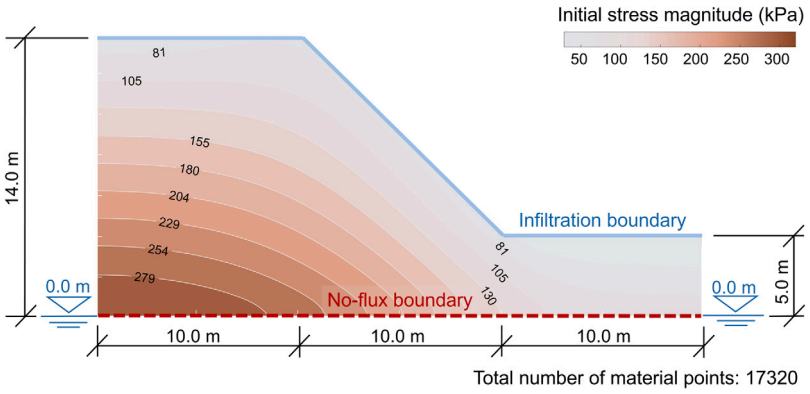


Fig. 9. Initial stress magnitude and geometry of the slope setup.

are used for every applied surface head and for both pore-gas treatments. This definition provides a consistent operational measure of the transition from small deformation to clear slope scale movement. Velocity, strain localization, and pore pressure are used to interpret the failure mechanism, but do not determine the reported onset time.

Fig. 9 shows the slope geometry, initial stress field, and particle discretization. Table 1 summarizes the mechanical, hydraulic, and numerical parameters. The parameter set is literature-based and represents a generic partially saturated embankment fill rather than a site-specific calibration. The baseline solid and liquid properties are adapted from the unsaturated MPM studies of Yerro et al. (2015) and Lei et al. (2021). The SWRC follows van Genuchten (1980), and the relative permeability functions follow Lewis and Schrefler (1998). Standard water and air properties at 17°C are used. The same model and parameters are applied in every paired simulation so that the comparison isolates the effect of evolving pore-gas pressure. The time step satisfies the stability conditions in Section 4.4, and the slope is discretized using 17,320 material points.

6.2. Comparison of macroscopic instability behaviour between modelling approaches

To establish the baseline response under weak hydraulic forcing, two simulations are performed with zero surface water head. The reference model follows Lei et al. (2021) and maintains pore-gas pressure at the atmospheric value. The reference discretization uses a grid spacing of 0.25 m, four material points per cell, and a time step of 1.0×10^{-4} s. Appendix examines the sensitivity of the paired results to the grid spacing, material point density, and time step. The coupled model solves the spatial and temporal evolution of P_g. Unless otherwise stated, pore-gas pressures are reported as gauge values relative to the standard atmospheric pressure, P_{atm} = 101 kPa, i.e., $P_g^{gauge} = P_g^{abs} - P_{atm}$.

Figs. 10 and 11 compare the liquid saturation and strain fields at t = 18 and 36 s. At t = 18 s, both simulations show limited deformation near the slope toe and only local differences in the wetting pattern. By t = 36 s, a continuous shear band has developed in both cases. The model with evolving P_g, however, produces a more confined mobilized zone, a narrower high strain region, and a shorter runout than the fixed P_g model.

Despite these differences after failure, the predicted onset times differ by less than 0.8 s. Under infiltration without surface ponding, pore-gas evolution therefore has little influence on failure initiation, although it affects local wetting and the subsequent deformation pattern. This behaviour is consistent with previous studies in which pore-gas remained secondary during rainfall infiltration without a sustained surface head (Cho et al., 2024; Iverson, 2000; Lei et al., 2021; Zhang et al., 2009). For this weak loading regime, prescribing atmospheric pore-gas pressure is therefore sufficient for predicting failure onset, but may not reproduce the same localization and run-out.

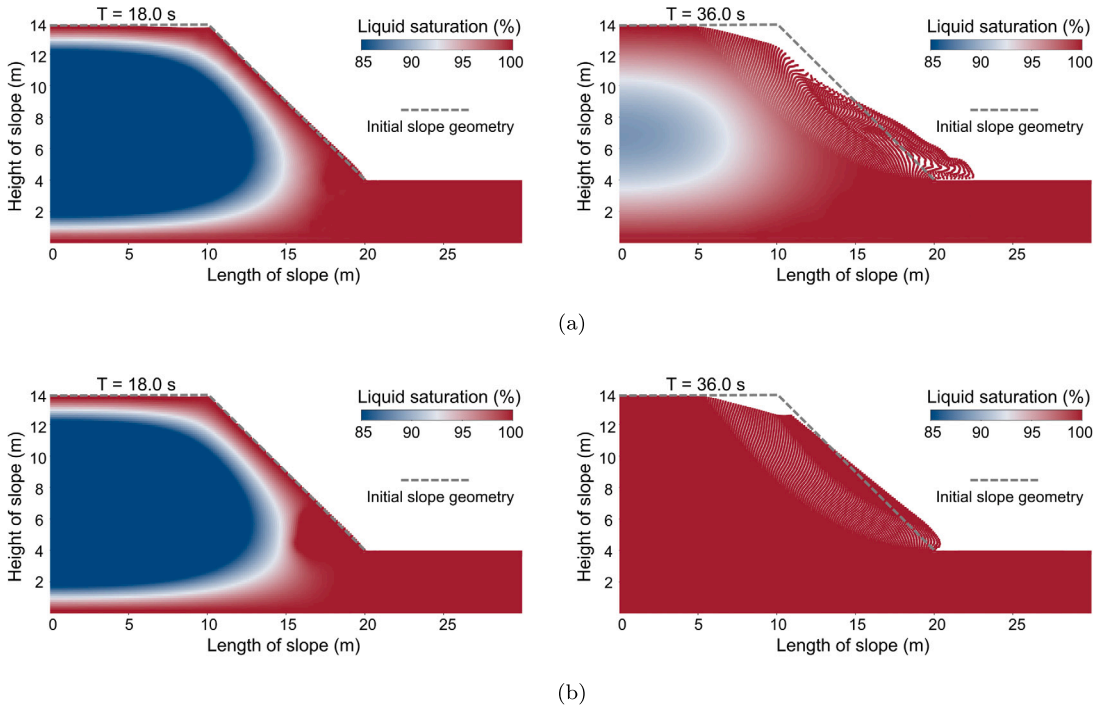


Fig. 10. Liquid-saturation fields at $t = 18$ s and $t = 36$ s under infiltration without surface ponding (zero surface water head): (a) prescribed-gas model following Lei et al. (2021) with fixed $P_g^{gauge} = 0$; (b) gas-coupled model with variable P_g.

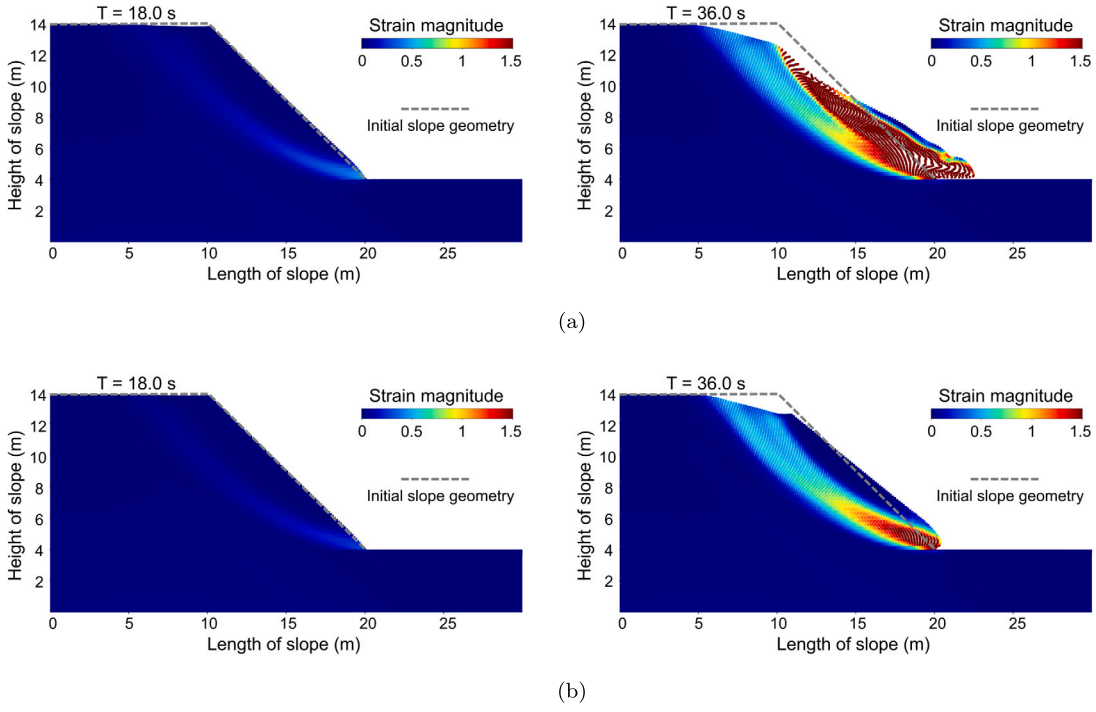


Fig. 11. Strain-magnitude fields at $t = 18$ s and $t = 36$ s for the two approaches: (a) prescribed-gas model; (b) gas-coupled model.

6.3. Reference behaviour under weak hydraulic forcing

The local gas response under weak forcing is examined in greater detail because the macroscopic fields show differences near the slope toe. With zero surface water head, variations in pore-gas pressure arise mainly from deformation-induced changes in pore volume rather than from external ponding.

Fig. 12(a) shows the absolute pore-gas pressure at $t = 18$ s. A localized pressure reduction develops near the toe, accompanied by smaller pressure increases along the slope surface and beneath the toe. This heterogeneous response shows that pore-gas pressure remains sensitive to local deformation even when it does not control the overall failure time.

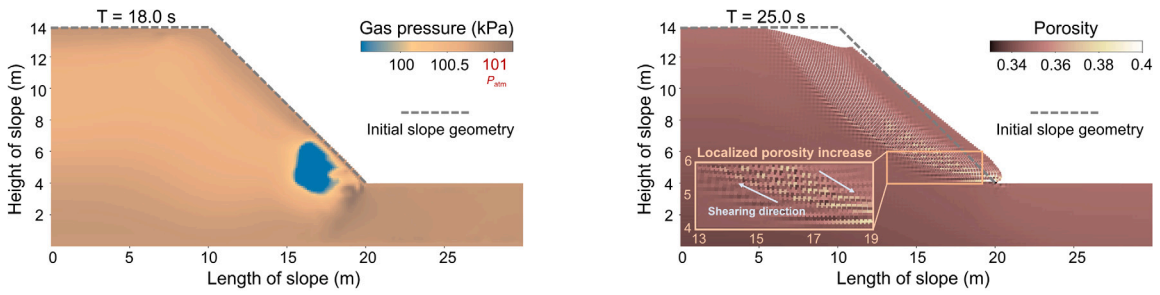


Fig. 12. Spatial distributions under weak hydraulic forcing: (a) absolute pore-gas pressure at t = 18 s (P_{atm} = 101 kPa); (b) porosity at t = 25 s, highlighting localized porosity increase within the developing sliding zone. The inset shows the averaging window, $13 \le x \le 19$ m and $4 \le y \le 6$ m.

Table 1
Material, hydraulic, and numerical parameters used in the unsaturated slope simulations.

Parameter	Description	Value
ρ_s	Solid density	2700 kg/m^3
E	Young's modulus	1×10^7 Pa
ν	Poisson's ratio	0.33
φ'	Effective friction angle	21°
c'	Effective soil cohesion	10 kPa
ψ	Dilation angle	0°
n	Porosity	0.35
k_a	Absolute intrinsic permeability	1.5×10^{-12} m^2
P_0	Reference pressure	100 kPa
ρ_l	Liquid density	1000 kg/m^3
S_l	Initial liquid saturation before gravity equilibration	0.4
S_{rl}	Residual liquid saturation	0.001
K_l	Liquid bulk modulus	1×10^8 Pa
μ_l	Liquid dynamic viscosity	1×10^{-3} Pa s
M_l	Liquid molar mass	0.018 kg/mol
ρ_g	Gas density at zero gauge pressure	1.29 kg/m^3
μ_g	Gas dynamic viscosity	1×10^{-5} Pa s
R	Universal gas constant	8.314 J/(mol K)
T	Absolute temperature	290.15 K (17°C)
M_g	Gas molar mass	0.029 kg/mol
S_g	Initial gas saturation before gravity equilibration	0.6
S_{rg}	Residual gas saturation	0.001
m	SWRC fitting parameter	0.3
m_l	Liquid relative-permeability parameter	2
m_g	Gas relative-permeability parameter	3
$\mathbf{g}$	Gravity	−9.81 m/s^2
Δt	Time step	1×10^{-4} s

The porosity field at t = 25 s in Fig. 12(b) shows that the same toe region subsequently experiences a localized increase in porosity. A similar porosity increase also occurs in the fixed P_g simulation. It is therefore associated with the evolving deformation field and formation of the incipient sliding zone, rather than being caused by pore-gas evolution. Because the dilation angle is zero in both models, this increase should not be interpreted as constitutive shear dilation. It reflects the total local deformation and geometric change represented by the large deformation formulation. When gas evolution is resolved, the local increase in pore volume produces an additional decompression response. The pore space expands faster than gas can redistribute or escape, causing a temporary decrease in P_g within the localized zone (Fredlund and Rahardjo, 1993). Comparable pressure reductions associated with rapid pore volume increase have been discussed for unsaturated porous media and deforming granular materials (Coussy, 2004b; Yerro et al., 2015; Yu et al., 2026).

The regional time histories in Fig. 13 are evaluated using material points within $13 \le x \le 19$ m and $4 \le y \le 6$ m. Within this window, particles are selected when their strain magnitude exceeds 0.3 at failure onset. For the zero head case, the onset time is 19.3 s and the nearest stored output at 19.5 s is used, retaining 70 material points. The region covers the localized toe failure zone and excludes surrounding material with limited deformation. A threshold sensitivity check confirms that 0.3 provides a suitable balance between localization and spatial representation. A threshold of 0.2 retains 246 particles and includes a broader peripheral region, whereas 0.4 retains only one particle. The intermediate value therefore captures the active shear band without reducing the average to an isolated point. The strain threshold is used only to identify the averaging region and does not determine failure onset, which is defined independently by the crest displacement criterion in Section 6.1.

Fig. 13(a) shows the evolution of pore-gas pressure and porosity within this region. In the model with evolving P_g, a sharp reduction develops near the failure onset interval ($t \approx 19.3$ s), concurrent with a rapid porosity increase. The fixed P_g model exhibits a similar porosity change but no gas pressure transient. This comparison confirms that local pore volume evolution occurs in both models, while transient decompression can only be represented when gas compressibility and transport are solved explicitly.

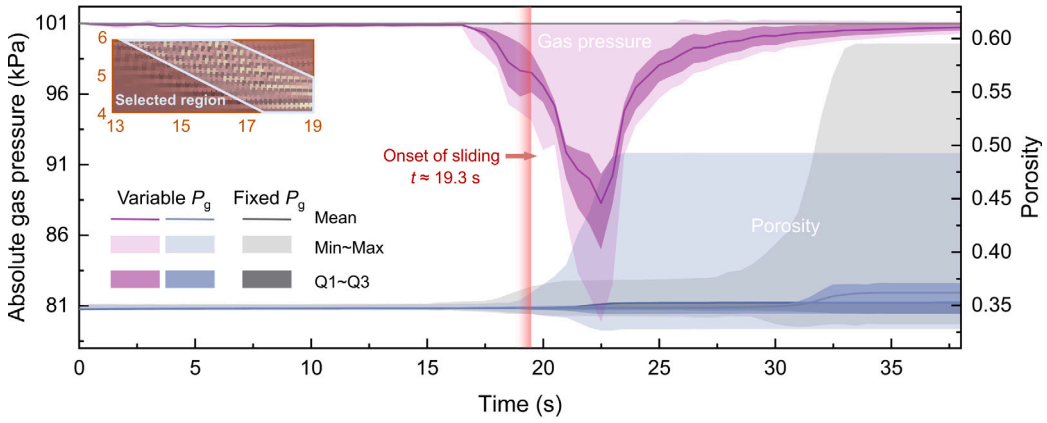
Fig. 13(b) compares the corresponding pore-water pressure and displacement. Pore-water pressure changes more smoothly than pore-gas pressure, although the model with evolving P_g shows a clearer transient fluctuation near failure onset. Its displacement increases rapidly and then approaches a plateau, whereas the fixed P_g model continues to accumulate movement over a longer period. Pore-gas pressure subsequently recovers towards the atmospheric value as pressure gradients relax and gas redistributes.

Under weak hydraulic forcing, pore-gas pressure therefore acts mainly as a transient response to localized pore volume change. It has little effect on failure onset but can modify pressure redistribution, localization, and movement after failure. This local interpretation is consistent with the macroscopic comparison in Section 6.2.

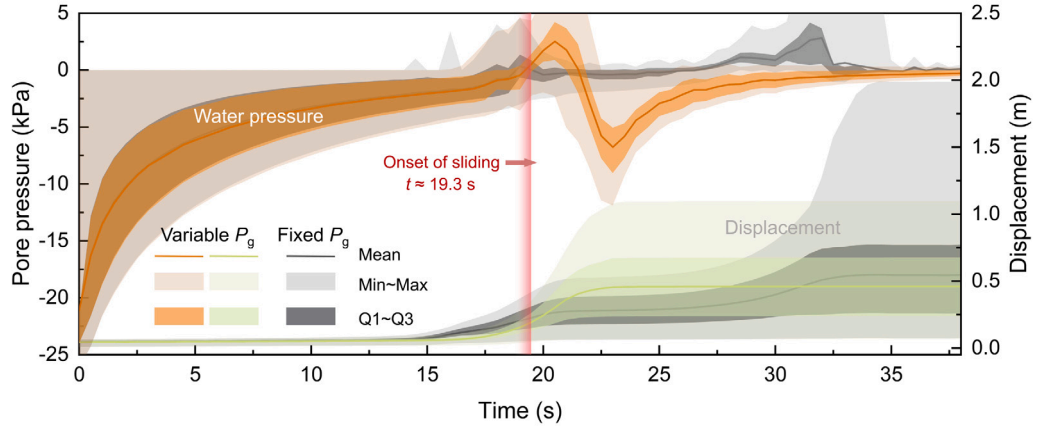
6.4. Transition from passive to active gas phase control with increasing hydraulic loading

The weak loading results show that pore-gas pressure is largely passive when no surface water head is present. To determine whether this remains true as hydraulic forcing increases, a series of paired simulations is performed with surface heads ranging from 0 to 2.5 m. The maximum head corresponds to approximately 25 kPa gauge pressure.

These loading levels are intended to represent rapid inundation rather than typical rainfall infiltration. The 2.5 m case probes the severe end of the range, such as intense overtopping or abrupt inundation during a typhoon. At elevated heads, the pore-water and pore-gas pressures are prescribed together at the submerged surface so that $P_c = P_g - P_l = 0$. This condition avoids retaining an artificial suction barrier at a submerged boundary. It represents temporary surface inundation with restricted direct venting to the atmosphere (Hu et al., 2024; Ma et al., 2019; Merry et al., 2006).

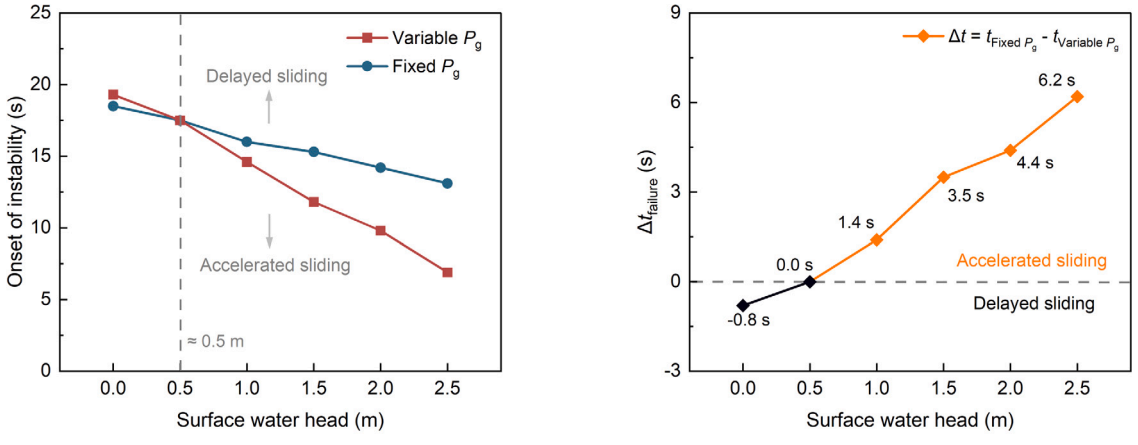


(a)



(b)

Fig. 13. Temporal evolution of local variables within the selected localized zone under weak hydraulic forcing, comparing simulations with variable P_g (coloured bands) and fixed P_g (grey bands): (a) absolute gas pressure and porosity; (b) pore-water pressure and displacement. Shaded regions indicate variability within the selected region (min–max and interquartile range). (For interpretation of the references to colour in this figure legend, the reader is referred to the web version of this article.)



(a) (b)

Fig. 14. Instability-onset transition with increasing surface water head: (a) onset time predicted by simulations with variable P_g and fixed P_g; (b) onset-time difference $\Delta t = t_{\text{fixed } P_g} - t_{\text{variable } P_g}$. Failure onset is defined by a downward displacement of 0.2 m at the monitoring material point located at the upper end of the inclined slope surface.

The resistance to water entry is driven primarily by the rapid rise in water pressure, rather than by the boundary condition alone. Water enters the pore space faster than gas can redistribute through the unsaturated fill and the hydraulically open side boundaries. Gas is therefore compressed ahead of the wetting front. The greater gas volume remains mainly in the partially saturated zone, whereas the near-surface region contains little gas after wetting.

Rapid overtopping and inundation are physically plausible loading scenarios, as discussed in the Introduction (Johnston et al., 2021; Zhou et al., 2022; Warmink et al., 2018; van Bergeijk, 2022). Nevertheless, the adopted surface condition is conservative because natural slopes may retain exposed or locally vented areas. Partial venting would reduce both the magnitude and duration of the pore-gas pressure peaks. The strong loading simulations should therefore be interpreted as a physically motivated upper bound rather than as a universal field boundary.

Fig. 14(a) shows the failure onset time as a function of surface head. At zero and 0.5 m, the two pore-gas treatments produce similar onset times, consistent with the passive response identified in Sections 6.2 and 6.3. From 1.0 m onward, the model with evolving P_g predicts progressively earlier failure as the imposed head increases. Fig. 14(b) quantifies this divergence using $\Delta t = t_{\mathrm{fixed},P_g} - t_{\mathrm{variable},P_g}$. The difference is slightly negative at zero head, is close to zero at 0.5 m, and becomes increasingly positive at higher heads. It reaches about 6 s at 2.5 m. Under the present configuration with restricted surface venting, this difference represents an upper bound for the adopted geometry, material properties, and loading history rather than a definitive field prediction.

Appendix examines whether the apparent crossover can be transferred to other hydraulic conditions. Using the supplementary global displacement criterion, the reference crossover is $H_c = 0.67$ m, with a range of 0.59–0.75 m for alternative onset thresholds. This result is consistent with the transition interval indicated by Fig. 14, although the values are not expected to coincide exactly because the main analysis and Appendix use different onset measures. More importantly, the sensitivity analysis shows that H_c can shift from below 0 m to above 2.5 m as intrinsic permeability, porosity, initial saturation, SWRC shape, and the surface gas boundary vary. The approximately 0.5–0.7 m crossover is therefore a nominal result for the reference configuration rather than a transferable hydraulic criterion.

The significance of Fig. 14 lies in the systematic change in behaviour rather than in a single threshold value. Under weak loading, gas pressure remains secondary. Under strong loading, gas compression and redistribution alter phase pressure partitioning and the effective stress within the developing shear band. Explicit gas evolution then becomes important for reproducing the relative failure timing under the conditions examined here.

6.5. Why shallower wetting can still lead to earlier failure

Section 6.4 shows that gas coupling advances failure under strong hydraulic loading. This result appears inconsistent with the established hydraulic effect of pore-gas, which resists water invasion and retards wetting front advance (Cho, 2016; Han et al., 2013; Kang et al., 2020; Liang et al., 2026). Shallower water penetration would normally be expected to preserve suction and delay weakening. The earlier failure predicted with evolving P_g therefore represents the infiltration paradox defined in the Introduction. The following analysis first establishes the hydraulic contrast, then examines phase pressure partitioning and the shear band stress path, and finally uses a control simulation to isolate the direct mechanical contribution of pore-gas.

6.5.1. Hydraulic retardation and phase pressure control underlying the infiltration paradox

Fig. 15 compares the early wetting response under a 2.5 m surface head. At $t = 5$ s, the wetting front in the model with evolving P_g is noticeably shallower than that in the fixed P_g model. The liquid saturation profiles in Fig. 16 show that this difference persists throughout the loading period.

The earlier failure of the model with evolving P_g therefore cannot be attributed to deeper wetting or greater saturation. If wetting-induced strength loss were the only controlling mechanism, this model should fail later. Figs. 15 and 16 instead establish the hydraulic side of the paradox: gas evolution retards water penetration, yet the slope fails earlier under strong loading.

The mechanical origin of the paradox is examined through the pressure contribution entering the Bishop effective stress relation. With saturation-based weighting, the mixture pressure is

$$\langle P_{\mathrm{mix}} \rangle = \langle S_l P_l \rangle + \langle S_g P_g \rangle, \qquad S_l + S_g = 1. \tag{81}$$

Here, angle brackets denote spatial averages over the toe region defined in Section 6.3 and illustrated in Fig. 13(a). The averages in Figs. 17 and 20 use 70 material points within the same window, $13 \le x \le 19$ m and $4 \le y \le 6$ m, identified using the strain magnitude threshold of 0.3. The same averaging window and number of material points are used for the two pore-gas treatments and the control comparison. The quantities $\langle S_l P_l \rangle$ and $\langle S_g P_g \rangle$ are averages of the particle-level products, rather than products of separately averaged saturation and pressure.

Fig. 17(a) presents the liquid and gas contributions as continuous curves and $\langle P_{\mathrm{mix}} \rangle$ at selected times as bars. In the model with evolving P_g, the gas contribution rises rapidly during the initial loading stage and then decreases as gas redistributes. The liquid contribution also rises faster and remains above that of the fixed P_g model. Consequently, $\langle P_{\mathrm{mix}} \rangle$ remains higher even after the direct gas term has largely dissipated. Pore-gas therefore affects the mixture pressure both directly through $\langle S_g P_g \rangle$ and indirectly by altering the liquid pressure response. Table 2 reports the phase pressure contributions in the evolving P_g model at its failure onset for each applied surface head. At zero head, the gas term is slightly negative because localized gas decompression offsets part of the positive liquid contribution. At 0.5 m, the gas term becomes positive and contributes 3.81% of $\langle P_{\mathrm{mix}} \rangle$. At 2.5 m, it reaches 398.7 Pa and accounts for 10.47% of the mixture pressure. The liquid phase remains dominant, but the additional gas contribution is sufficient to alter a stress state already approaching failure. Across the head series, failure onset occurs progressively earlier and the absolute gas contribution increases monotonically. The 2.5 m case is therefore used for the detailed mechanical analysis in Figs. 17 and 18 because it exhibits the largest gas contribution and the clearest difference between the two models. Table 2 establishes the systematic trend across the complete loading range, while the figures provide a representative mechanistic case.

Fig. 18 shows the spatial distribution of gas volume and the pressure contributions $S_g P_g$ and $S_l P_l$. The liquid term broadly follows the wetting front, whereas the gas term becomes concentrated around the developing shear band. Elevated pore-gas pressure near the surface does not imply that a large gas volume is stored there. The near-surface region contains little gas after wetting, while the larger gas-filled zone remains ahead of the wetting front. The surface signal should therefore be interpreted as a transient pressure response within a small remaining gas volume, rather than as local gas accumulation. Although the direct gas contribution is transient and spatially confined, gas evolution modifies the liquid pressure field through the coupled hydraulic and mechanical response. The mixture pressure therefore remains elevated after $\langle S_g P_g \rangle$ has declined.

Under the adopted stress sign convention,

$$\boldsymbol{\sigma}' = \boldsymbol{\sigma} + P_{\mathrm{mix}}\mathbf{I}, \qquad p' = -\frac{1}{3}\mathrm{tr}(\boldsymbol{\sigma}') = -\frac{1}{3}\mathrm{tr}(\boldsymbol{\sigma}) - P_{\mathrm{mix}} \tag{82}$$

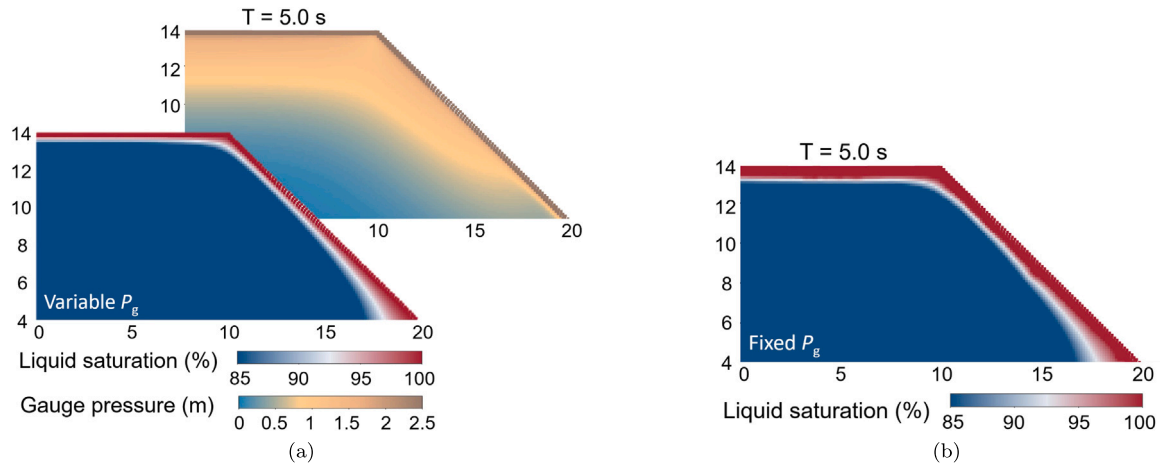


Fig. 15. Early-stage wetting under a 2.5 m surface water head (≈25 kPa gauge) at $t = 5$ s: (a) variable P_g simulation showing liquid saturation and gas pressure; (b) fixed P_g simulation showing liquid saturation.

Table 2
Phase pressure contributions in the evolving P_g model at failure onset under different surface water heads. The averages are evaluated using the 70 material points in the region defined in Section 6.3.

Surface head (m)	Onset time (s)	Liquid term $\langle S_l P_l \rangle$ (Pa)	Gas term $\langle S_g P_g \rangle$ (Pa)	$\langle P_{mix} \rangle$ (Pa)	Liquid:gas (%)
0.0	19.3	275.5	−2.9	272.6	101.05 : −1.05[a]
0.5	17.5	298.9	11.8	310.7	96.19 : 3.81
1.0	14.6	1258.2	35.3	1293.4	97.27 : 2.73
1.5	11.8	1882.8	74.8	1957.6	96.18 : 3.82
2.0	9.8	2732.4	152.8	2885.2	94.70 : 5.30
2.5	6.9	3407.6	398.7	3806.3	89.53 : 10.47

[a] At zero surface water head, the negative gas contribution reflects transient gas decompression and offsets part of the liquid contribution. The percentages are therefore reported as signed contributions to P_{mix}.

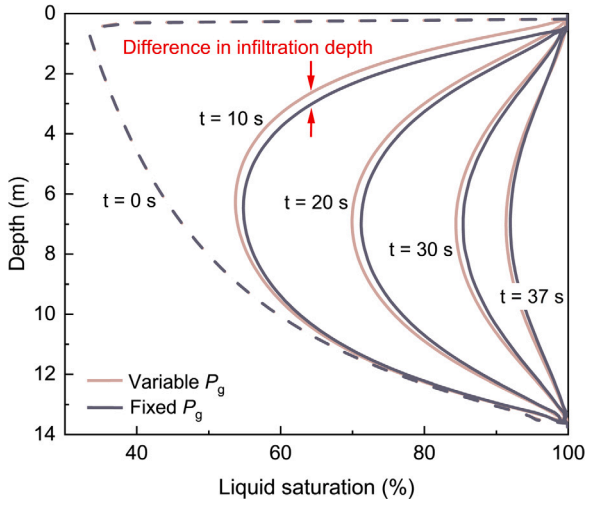


Fig. 16. Depth-wise liquid-saturation profiles ($x = 5$ m) under a 2.5 m surface water head at representative times ($t = 0$, 10, 20, 30, and 37 s), comparing variable P_g and fixed P_g simulations.

An increase in P_{mix} therefore reduces the mean effective stress within the shear band. Fig. 17(b) shows that the mean effective stress decreases more rapidly when P_g is allowed to evolve, and failure begins at approximately 6.9 s. The fixed P_g model undergoes a slower stress reduction and reaches failure at approximately 13.1 s. After onset, the effective stress partly recovers as the initial gas contribution dissipates and the local stress field redistributes.

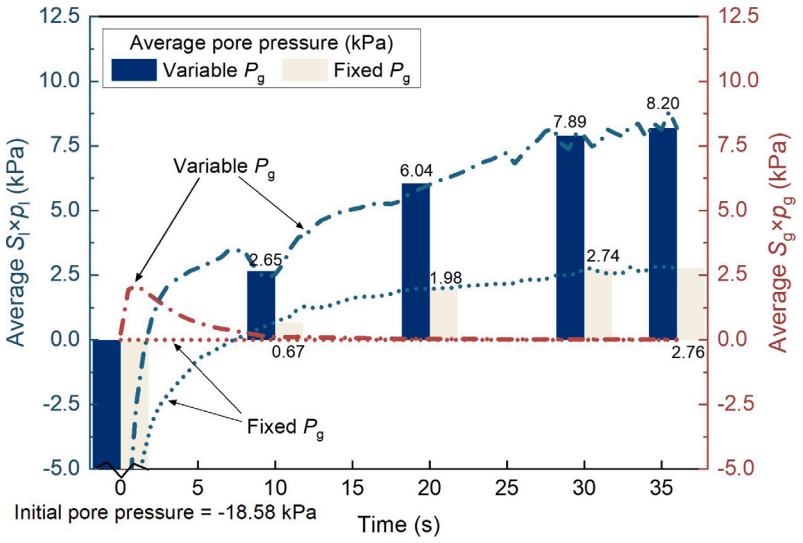
The strain histories show that pore gas mainly advances the onset of localization rather than producing a uniformly larger strain throughout the simulation. At approximately 10 s, the average strain magnitude is 1.10 in the model with evolving P_g, compared with 0.07 in the fixed P_g model. The difference becomes less systematic at later times. Fig. 19 further shows that failure occurs at a lower average liquid saturation but with more rapid strain localization when gas evolution is resolved.

These results demonstrate that failure under strong hydraulic loading cannot be explained by wetting front advance alone. Transient gas compression modifies both the direct gas contribution and the liquid pressure response, shifts the effective stress path, and advances localization within the shear band.

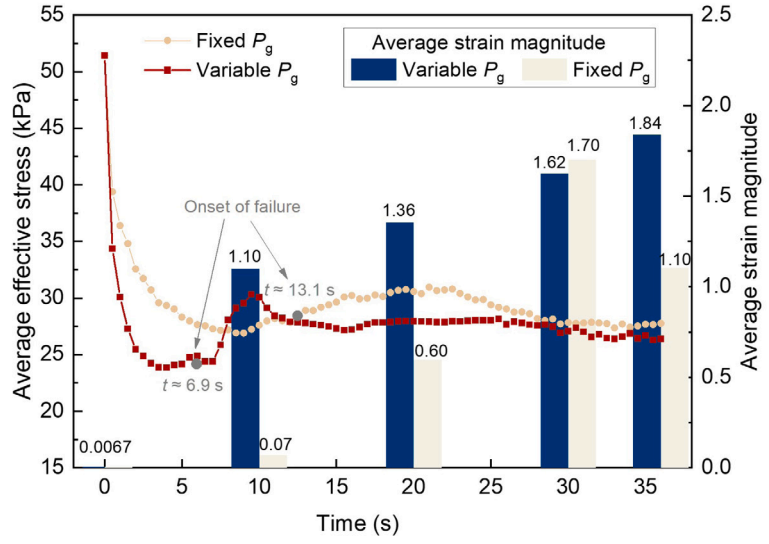
6.5.2. Control test isolating the direct mechanical contribution of pore-gas

A diagnostic control simulation is performed under the same 2.5 m surface head to separate the direct stress contribution of pore-gas from its remaining hydraulic effects. The governing equations, pressure update, boundary conditions, and pore-gas evolution are unchanged. The only modification is that the gas weighting coefficient in the effective stress relation is set to zero, $\chi_g = 0$. Pore-gas pressure is therefore still solved and continues to influence suction, saturation, permeability, water entry, and pressure redistribution. Only its direct contribution to the skeleton effective stress is removed. This control case is not proposed as an alternative constitutive model; it is used solely to identify the mechanical pathway associated with the gas pressure term. Fig. 20(a) compares the pressure contribution entering the effective stress relation in the full model and the $\chi_g = 0$ control, using the same 70-point averaging region described in Section 6.5.1. In the full model, this contribution rises more rapidly and remains higher during the critical stage before failure. Setting $\chi_g = 0$ weakens the pressure response, showing that the direct gas term amplifies the reduction in local effective stress. Because the system is close to localization, even a moderate change in the stress path can affect the onset time.

Fig. 20(b) shows the corresponding displacement histories. The full model exhibits an earlier transition to rapid displacement, whereas the



(a)



(b)

Fig. 17. Shear band diagnostics under a 2.5 m surface water head: (a) spatially averaged phase pressure contributions $\langle S_l P_l \rangle$ and $\langle S_g P_g \rangle$, together with $\langle P_{mix} \rangle$ at selected times; (b) average mean effective stress and strain magnitude within the shear band for the variable and fixed P_g simulations.

control case delays this acceleration. The result confirms that the direct gas contribution to effective stress actively promotes earlier localization under strong loading.

The infiltration paradox therefore arises from competing hydraulic and mechanical effects. Gas pressure retards wetting front advance, which tends to delay failure, but its direct and indirect influence on the shear band stress path promotes earlier localization. Under the present strong loading condition, the mechanical effect becomes dominant, and the slope fails earlier despite a shallower wetting front.

6.6. Broader implications and conceptual interpretation

Fig. 21 complements the slope scale loading diagram in Fig. 1a by showing how the mechanical role of pore-gas changes as hydraulic forcing increases. The results do not indicate a uniform gas effect. Instead, they define three regimes governed by the competition between the rate of hydraulic loading and the capacity of gas to redistribute or vent.

Under weak infiltration without surface ponding, gas pressure responds mainly to local deformation and pore volume change. The response is short-lived and has little effect on failure onset. In this hydraulically dominated regime, a model that prescribes atmospheric P_g can provide a reasonable estimate of failure timing, although it may not reproduce the same localization or movement after failure. As surface ponding develops, the hydraulic loading and gas redistribution timescales become comparable. Local pore volume changes within the developing shear band can no longer be equilibrated immediately. The resulting pressure disequilibrium begins to alter phase pressure partitioning and the local stress path. This transition produces measurable differences in deformation and, beyond a configuration-dependent loading level, in failure onset. Under strong loading, the water pressure rises faster than gas can escape. Gas compression develops ahead of the wetting front and contributes directly and indirectly to the reduction in effective stress. Failure timing is then governed less by wetting depth alone and more by the transient stress redistribution produced

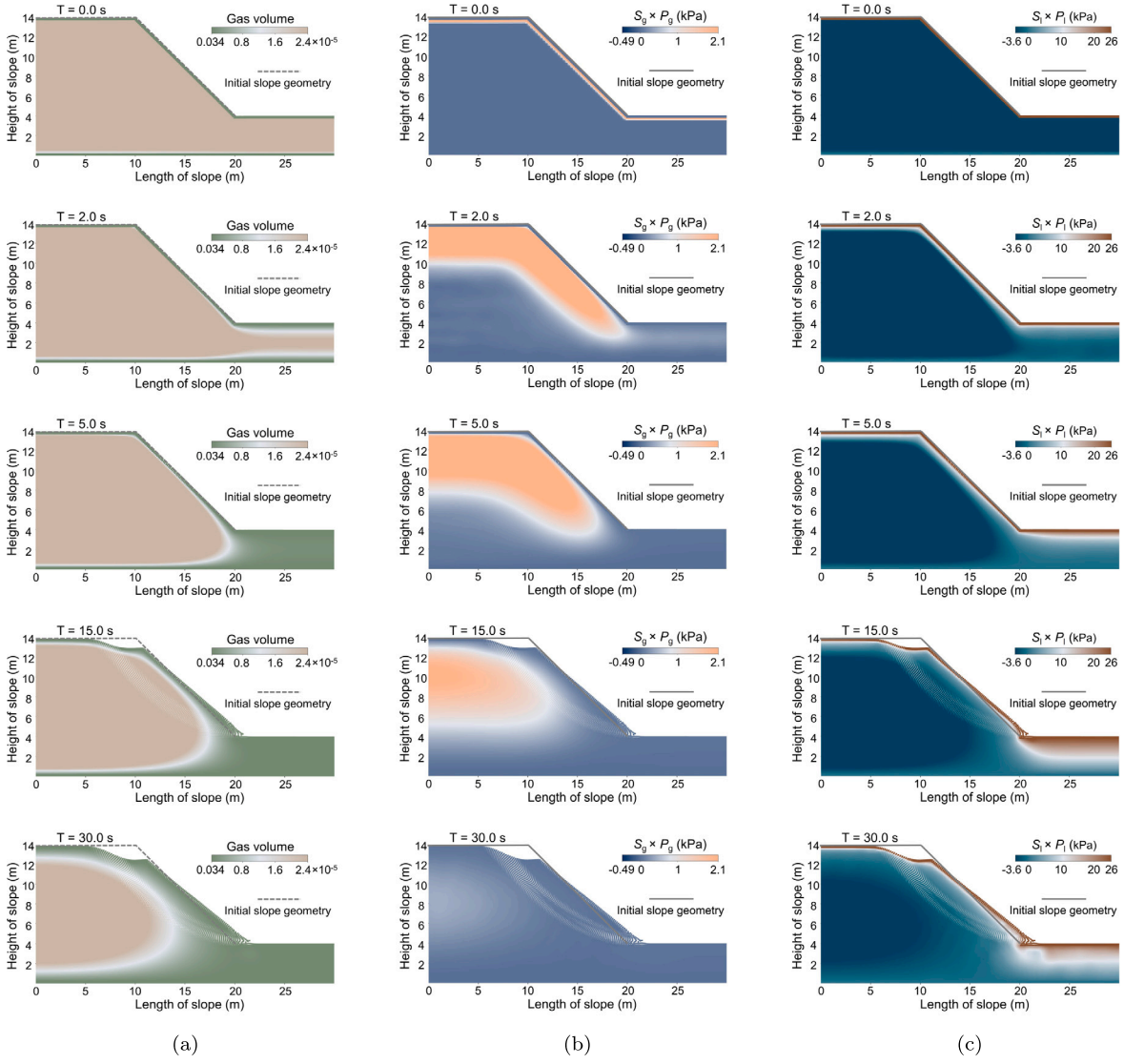


Fig. 18. Slope response under a 2.5 m surface water head: (a) gas volume; (b) $S_g \times P_g$; (c) $S_l \times P_l$ at representative times.

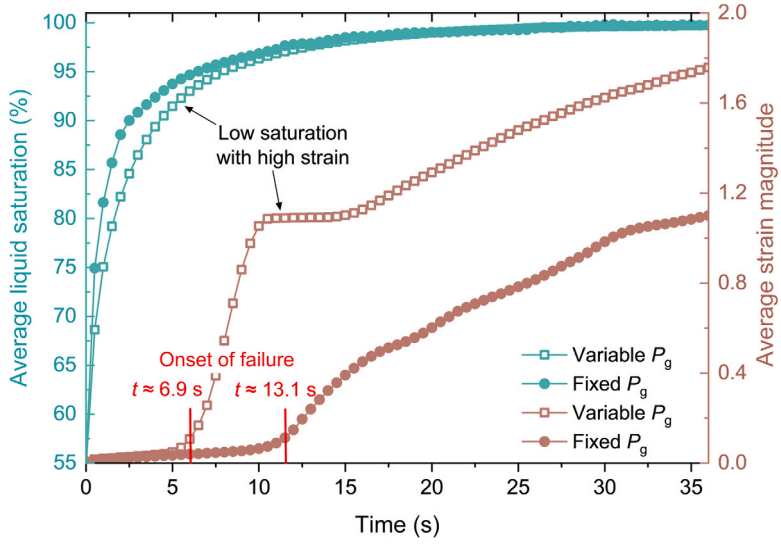


Fig. 19. Co-evolution of shear-band average liquid saturation and strain magnitude, comparing variable-P_g and fixed-P_g simulations; failure occurs at lower saturation but higher localization rate in the variable-P_g case.

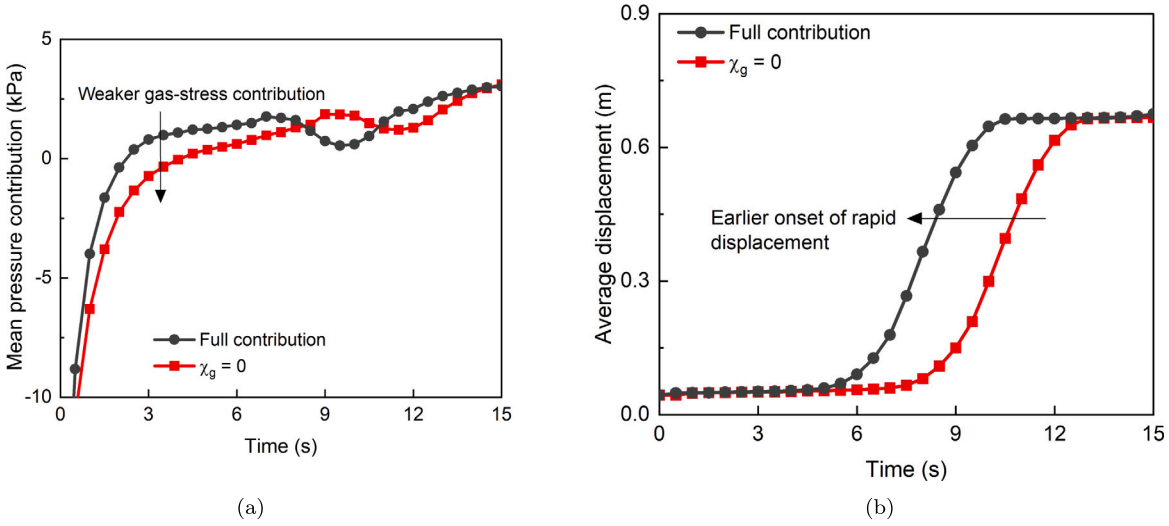


Fig. 20. Control test under a 2.5 m surface water head, in which χ_g is set to zero only in the effective-stress evaluation while pore-gas pressure evolution and all other model settings are kept unchanged: (a) average pressure contribution entering the effective-stress relation; (b) average displacement in the selected shear-band region.

by coupled solid, liquid, and gas interaction. This mechanism explains why the slope can fail earlier even though water penetration remains shallower. The results provide a practical basis for selecting the required level of hydraulic modelling. Explicit three-phase coupling is most justified for initially unsaturated fills subjected to rapid reservoir filling, overtopping, abrupt ponding, or rapid inundation, particularly where a low permeability surface crust, low gas mobility, or restricted lateral venting limits gas release. Under these conditions, the hydraulic loading timescale may be shorter than the gas equilibration timescale, making the atmospheric gas assumption unreliable.

A two-phase approach may remain adequate for gradual rainfall, highly permeable or well-vented fills, or nearly saturated soils in which little compressible gas remains and P_g stays close to atmospheric pressure. For the reference configuration, the crossover occurs over a narrow interval near 0.5–0.7 m. Appendix shows, however, that this value can shift from below 0 m to above 2.5 m as the hydraulic properties, initial state, and surface gas boundary vary. The crossover should therefore not be used as a transferable design threshold. The broader model selection criterion is whether the hydraulic loading timescale is shorter than the time required for pore-gas to redistribute or vent. Fig. 21 summarizes this regime-based interpretation and indicates when the additional computational cost of explicitly resolving pore-gas may be justified.

7. Conclusions

This study investigated how evolving pore-gas pressure affects failure initiation in partially saturated slopes subjected to increasing surface hydraulic loading. A three-phase hydro-mechanical MPM was used to compare simulations that explicitly resolve pore-gas pressure with otherwise identical simulations in which P_g remains atmospheric. The main conclusions are as follows.

(1) Under weak hydraulic loading with zero surface water head, pore-gas pressure acts mainly as a transient response to localized pore volume change. The predicted failure onset times differ by less than 0.8 s between the two models, although the wetting pattern, strain localization, and run-out remain different. Prescribing atmospheric pore-gas pressure is therefore adequate for predicting failure onset in this regime, but may not reproduce the subsequent deformation pattern.

(2) Increasing the surface water head produces a transition from passive to active gas control. In the reference configuration, the ordering of the two predictions changes over a narrow head interval near 0.5–0.7 m. At a surface head of 2.5 m, the model with evolving P_g predicts failure about 6 s earlier than the fixed P_g model. Because this case combines severe loading with restricted surface venting, the difference represents an upper bound for the present configuration. The sensitivity analysis shows that the crossover can shift from below 0 m to above 2.5 m as the hydraulic properties, initial state, and gas boundary condition vary. It should therefore not be interpreted as a general design value.

(3) The infiltration paradox arises from competition between hydraulic retardation and mechanical acceleration. Gas compression and redistribution hinder water penetration and maintain a shallower wetting front, but also increase the phase-weighted mixture pressure. This increase occurs directly through the gas term and indirectly through the modified liquid pressure response. At failure onset, the gas term contributes 3.81% of P_{mix} at a head of 0.5 m and 10.47% at 2.5 m, although the liquid contribution remains dominant. The resulting increase in P_{mix} reduces the mean effective stress and advances strain localization within the developing shear band. The control simulation with $\chi_g = 0$ confirms that the direct contribution of gas to effective stress promotes earlier failure, while the remaining hydraulic effects of the gas evolution also contribute to the response.

(4) The results provide a practical basis for selecting the required level of multiphase modelling. Explicit three-phase coupling is most relevant when hydraulic loading develops faster than pore-gas can redistribute or vent. Such conditions may arise during rapid reservoir filling, wave overtopping, abrupt ponding, or rapid inundation of initially unsaturated fills, particularly where low gas mobility, a low permeability surface crust, or restricted venting limits pressure release. A two-phase approach may remain adequate under gradual rainfall, highly permeable or well-vented conditions, or nearly saturated states in which little compressible gas remains.

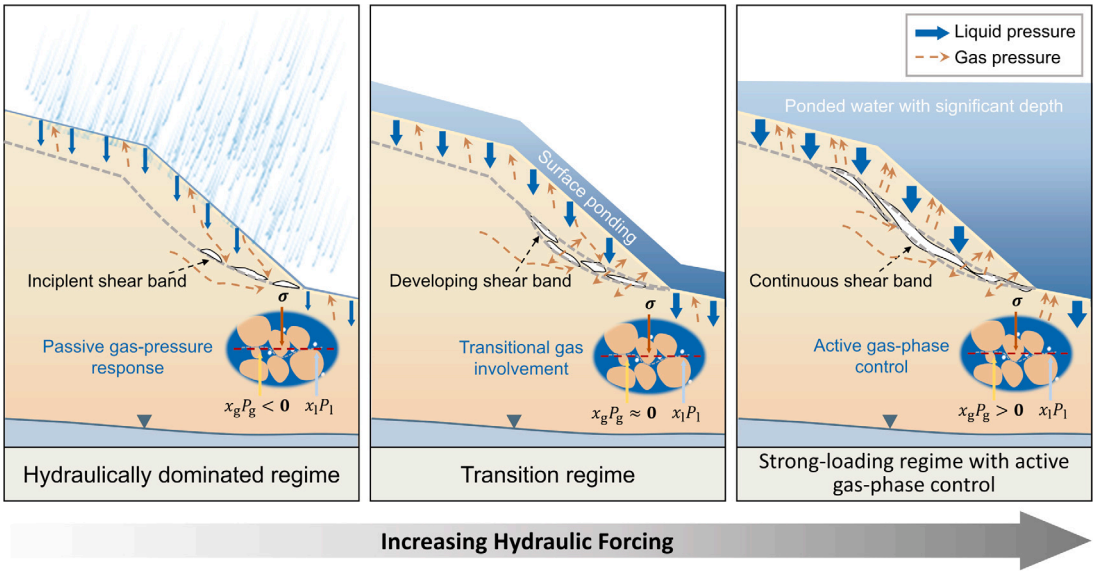


Fig. 21. Conceptual framework illustrating the regime-dependent role of gas-phase behaviour in slope failure under increasing hydraulic forcing.

The quantitative results are specific to the present 2D plane strain model, homogeneous soil, idealized hydraulic boundaries, restricted surface venting, and literature-based parameter set. Appendix shows that the crossover head depends on the configuration and that the absolute onset times remain sensitive to numerical resolution, although the earlier onset predicted with evolving P_g persists across the tested numerical settings. The mass-balance assessment is limited to the reported loading case. The constitutive setting is intended for a controlled comparison rather than a site-specific calibration. Future work should examine parameter interactions, field heterogeneity, advanced constitutive descriptions, and mixed gas boundaries that permit partial venting.

CRediT authorship contribution statement

Xiaoying Chen: Writing – original draft, Visualization, Validation, Software, Methodology, Investigation, Formal analysis, Data curation, Conceptualization. **Jidong Zhao:** Writing – review & editing, Validation, Supervision, Project administration, Methodology, Investigation, Funding acquisition, Formal analysis, Conceptualization. **Jidu Yu:** Writing – review & editing, Validation, Software, Methodology, Investigation, Formal analysis.

Declaration of competing interest

The authors declare that they have no known competing financial interests or personal relationships that could have appeared to influence the work reported in this paper.

Acknowledgements

This work was financially supported by the National Natural Science Foundation of China (Project No. 52439001), the Research Grants Council of Hong Kong (GRF Projects No. 16214525 and No. 16217225, CRF Project No. C7085-24G, and TRS Projects No. T22-606/23-R and No. T22-607/24N), and the State Key Laboratory of Climate Resilience for Coastal Cities (SKLCRCC) (via Project ITC-SKLCRCC26EG01). Any opinions, findings, conclusions or recommendations expressed in this material are those of the authors and do not necessarily reflect the views of the funding agencies.

Appendix. Parametric and numerical sensitivity assessment

A.1. Sensitivity of the crossover head

A one-factor-at-a-time sensitivity analysis was conducted to determine whether the transition between the two pore-gas treatments can be transferred to other hydraulic conditions. The parameters considered were intrinsic permeability, porosity, initial liquid saturation, the SWRC shape parameter m, and the ratio between the prescribed surface gas and liquid pressures. Each parameter was examined at three levels while the slope geometry, strength parameters, and remaining inputs were held constant.

The main analysis in Section 6 defines failure onset using the downward displacement of the monitored crest material point. For the sensitivity assessment, a global displacement measure was used to permit consistent comparison among parameter sets. Onset was defined by an increase in the 99th percentile particle displacement of Δu_{99} = 0.20 m relative to the gravity-equilibrated state. Results obtained using thresholds of 0.15 and 0.25 m were used to evaluate the sensitivity of the detected transition. This supplementary metric does not replace the crest-based definition used for the main results. The global measure reduces dependence on a single monitoring particle when the grid spacing or material point density changes. Both the main crest-based analysis and the supplementary global measure predict earlier onset with evolving P_g under the 2.5 m surface head, although the absolute onset times and the inferred crossover head differ. The crossover head H_c is defined as the surface head at which $\Delta t = t_{\text{fixed } P_g} - t_{\text{variable } P_g}$ changes sign. Its value was obtained by linear interpolation between adjacent surface heads. Cases in which no sign change occurred over the tested interval of 0–2.5 m are reported as bounds rather than extrapolated values.

Fig. A.22 shows that H_c is configuration dependent. The reference configuration gives H_c = 0.67 m, with a range of 0.59–0.75 m for the alternative onset thresholds. Across all tested conditions, the crossover varies from below 0 m to above 2.5 m. Intrinsic permeability exerts a particularly strong influence: reducing the permeability to $0.1k_{\text{ref}}$

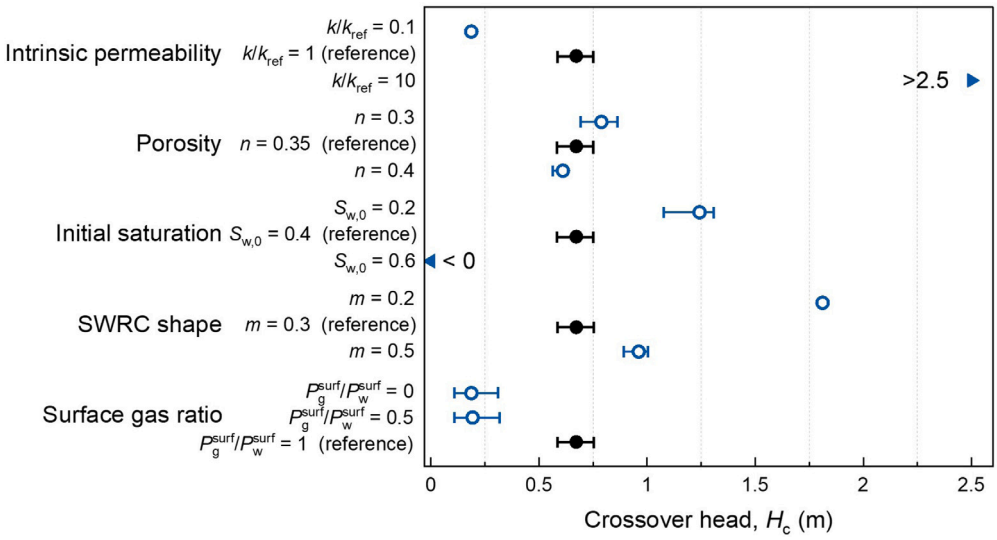


Fig. A.22. Parametric sensitivity of the crossover head H_c. Markers denote results obtained using the nominal onset definition $\Delta u_{99} = 0.20$ m, and horizontal bars indicate the range for thresholds of 0.15–0.25 m. Black markers indicate reference values. Arrowheads (<0, >2.5) denote censored cases with no crossover within the tested range. The surface gas ratio is defined as the ratio of prescribed surface gas pressure to surface water pressure.

lowers H_c to approximately 0.19 m, whereas no crossover occurs below 2.5 m at $10k_{ref}$. Initial saturation and SWRC shape also produce substantial shifts, while porosity causes a more moderate change. Altering the surface gas pressure ratio similarly moves the crossover away from the reference value.

These results confirm that the approximately 0.5 m transition identified from the original head series is a nominal response of the reference configuration rather than a transferable design criterion. The broader interpretation remains that the role of pore-gas is governed by the competition between the imposed hydraulic loading and the ability of gas to compress, redistribute, or vent.

A.2. Numerical robustness of the paired slope simulations

A numerical assessment was conducted for the slope subjected to a 2.5 m surface head. Grid spacing, material point density, and time step were varied separately. The reference setting used in the main simulations consists of $h = 0.25$ m, four material points per cell, and a time step of $\Delta t = 1.0 \times 10^{-4}$ s. These settings are consistent with the reference slope calculation of Lei et al. (2021), allowing the present prescribed and evolving P_g simulations to be compared under the same numerical basis.

Fig. A.23(a) shows that the coarse grid with $h = 0.5$ m predicts substantially earlier onset in both models, indicating insufficient resolution of the developing deformation zone. Refinement from the reference grid, $h = 0.25$ m to 0.125 m, produces much smaller changes. The variable P_g onset changes from approximately 6.7 to 7.1 s, while the fixed P_g onset changes from about 12.2 to 12.6 s. The corresponding onset time difference remains close to 5.5 s. The reference grid therefore reproduces the relative response obtained using the finer grid, although the coarse grid does not. Increasing the material point density delays the absolute onset times, particularly between one and four material points per cell, as shown in Fig. A.23(b). However, the onset time difference is similar for four and nine material points per cell, at approximately 5.44 and 5.27 s, respectively. The comparative effect of pore-gas evolution is therefore less sensitive to material point density than the individual onset times.

The variable P_g onset changes by less than 0.2% as the time step decreases from 1×10^{-4} to 2.5×10^{-5} s, as shown in Fig. A.23(c). The fixed P_g result shows greater time step sensitivity, but the variable P_g model reaches the onset criterion first for every tested time step. The results therefore support the robustness of the relative ordering, while the precise onset times remain dependent on numerical resolution. Fig. A.23(d) evaluates global mass balance over 0–20 s for the evolving P_g simulation under a 2.5 m surface head, using the hydraulic boundary conditions described in Sections 6.1 and 6.4. Because these boundaries permit fluid exchange, changes in the domain mass inventories alone are not conservation errors. The relative mass-balance residual is defined as

$$\mathcal{M}_\alpha(t) = \sum_{p=1}^{N_p} m_{\alpha,p}(t),$$
$$\varepsilon_\alpha(t) = \frac{\mathcal{M}_\alpha(t) - \mathcal{M}_\alpha(0) - B_\alpha(t)}{\mathcal{M}_\alpha(0)} \times 100\%, \qquad \alpha = \mathrm{l, g}. \tag{A.1}$$

Here, $m_{\alpha,p}(t)$ is the current mass of phase α at material point p, N_p is the total number of material points, and $t = 0$ denotes the start of hydraulic loading after gravity equilibration. The cumulative net boundary transfer $B_\alpha(t)$ is obtained by integrating the net mass flux across the computational boundary over time, with net inflow taken as positive. The total fluid residual is calculated by summing the liquid and gas masses and boundary transfers before normalization. The flux-corrected residuals remain close to zero over the reported interval, supporting global phase mass balance for the evaluated infiltration case.

Overall, the reference discretization supports the controlled comparison undertaken here. The earlier onset predicted with evolving P_g persists across the tested grid, material point, and time step settings. This comparative ordering is more robust than the absolute onset times. The analysis therefore supports the principal mechanism-based conclusion without implying complete numerical convergence or universal quantitative prediction.

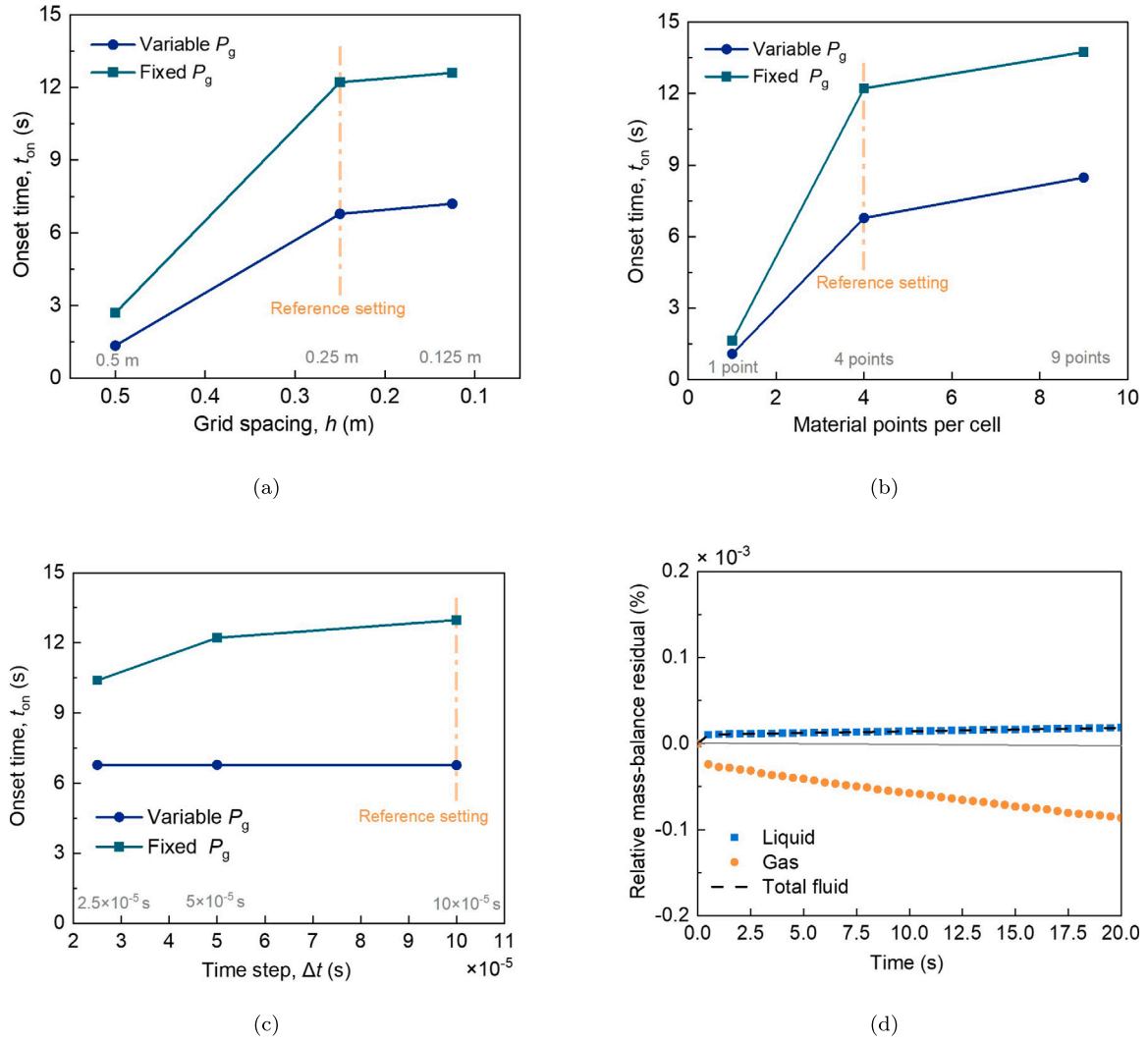


Fig. A.23. Numerical assessment of the slope under a 2.5 m surface water head: (a) sensitivity of failure onset to grid spacing; (b) sensitivity to material point density; (c) sensitivity to the time step; and (d) relative mass-balance residuals for the liquid, gas, and total fluid after accounting for cumulative boundary mass transfers. The orange dashed lines in (a)–(c) identify the reference numerical settings. Residuals in (d) are normalized by the corresponding initial masses and evaluated using the hydraulic boundary conditions of the infiltration simulation.

Data availability

Data will be made available on request.

References

Alonso, E.E., Gens, A., Delahaye, C.H., 2003. Influence of rainfall on the deformation and stability of a slope in overconsolidated clays: a case study. Hydrogeol. J. 11 (1), 174–192. http://dx.doi.org/10.1007/s10040-002-0245-1.

Bandara, S., Ferrari, A., Laloui, L., 2016. Modelling landslides in unsaturated slopes subjected to rainfall infiltration using material point method. Int. J. Numer. Anal. Methods Geomech. 40 (9), 1358–1380. http://dx.doi.org/10.1002/nag.2499.

Ceccato, F., Yerro, A., Di Carluccio, G., 2024. Simulating landslides with the material point method: best practices, potentialities, and challenges. Eng. Geol. 338, 107614. http://dx.doi.org/10.1016/j.enggeo.2024.107614.

Cho, S.E., 2016. Stability analysis of unsaturated soil slopes considering water-air flow caused by rainfall infiltration. Eng. Geol. 211, 184–197. http://dx.doi.org/10.1016/j.enggeo.2016.07.008.

Cho, M.T.T., Sato, T., Saito, H., Izumi, A., Kohgo, Y., 2024. Effects of pore water and pore air pressure on the slope failure mechanisms due to rainfall in centrifuge investigation. Geoenvironmental Disasters 11 (1), 40. http://dx.doi.org/10.1186/s40677-024-00305-5.

Coussy, O., 2004a. Deformation and kinematics. In: Poromechanics. John Wiley & Sons, Chichester, pp. 1–18. http://dx.doi.org/10.1002/0470092718.ch1, Chapter 1.

Coussy, O., 2004b. Unsaturated thermoporoelasticity. In: Poromechanics. John Wiley & Sons, Chichester, pp. 151–187. http://dx.doi.org/10.1002/0470092718.ch6, Ch. 6.

Cui, W.J., Potts, D.M., Zdravkovic, L., Gawecka, K.A., Taborda, D.M.G., 2018. An alternative coupled thermo-hydro-mechanical finite element formulation for fully saturated soils. Comput. Geotech. 94, 22–30. http://dx.doi.org/10.1016/j.compgeo.2017.08.011.

de la Cruz, V., Sahay, P.N., Spanos, T.J.T., 1993. Thermodynamics of porous media. In: Proceedings of the Royal Society of London. In: Series A: Mathematical and Physical Sciences, vol. 443, pp. 247–255. http://dx.doi.org/10.1098/rspa.1993.0143.

Di Carluccio, G., Aviles, L.A., Pinyol, N.M., Alonso, E.E., 2025. Modelling wetting collapse, failure and deposition of an unsaturated slope with material point method. Int. J. Numer. Anal. Methods Geomech. 49, 4526–4551. http://dx.doi.org/10.1002/nag.70075.

Ehlers, W., 2002. Foundations of multiphasic and porous materials. In: Porous Media: Theory, Experiments and Numerical Applications. Springer Berlin Heidelberg, Berlin, Heidelberg, pp. 3–86. http://dx.doi.org/10.1007/978-3-662-04999-0_1.

Fredlund, D.G., Rahardjo, H., 1993. Pore pressure parameters. In: Soil Mechanics for Unsaturated Soils. Wiley, New York, pp. 178–216. http://dx.doi.org/10.1002/9780470172759.ch8.

Gu, X.Y., Dong, C.Y., Cheng, T., Zhang, Y., Bai, Y., 2016. The transient heat conduction MPM and GIMP applied to isotropic materials. Eng. Anal. Bound. Elem. 66, 155–167. http://dx.doi.org/10.1016/j.enganabound.2016.02.009.

Han, T.C., Ma, S.G., Xu, R.Q., 2013. Research on delayed effect of landslides caused by air pressure under heavy rainfall. Rock Soil Mech. 34, 1360–1366.

Hidano, S., Yamaguchi, Y., Takase, S., Moriguchi, S., Kaneko, K., Terada, K., 2024. Semi-implicit material point method for simulating infiltration-induced failure of

unsaturated soil structures. Int. J. Numer. Anal. Methods Geomech. 48 (10), 2661–2699. http://dx.doi.org/10.1002/nag.3750.
Higo, Y., Takegawa, Y., Zhu, F., Uchiyama, D., 2025. A three-phase two-point MPM for large deformation analysis of unsaturated soils. Comput. Geotech. 177, 106860. http://dx.doi.org/10.1016/j.compgeo.2024.106860.
Hu, J., Chen, Y.M., Li, J.H., Ke, H., Li, J.C., 2024. Centrifuge modeling of slope failure induced by elevated gas pressure in wet municipal solid waste landfill. Can. Geotech. J. 61 (6), 1094–1108. http://dx.doi.org/10.1139/cgj-2023-0048.
Hu, R., Chen, Y.F., Zhou, C.B., 2011. Modeling of coupled deformation, water flow and gas transport in soil slopes subjected to rain infiltration. Sci. China Technol. Sci. 54 (10), 2561–2575. http://dx.doi.org/10.1007/s11431-011-4504-z.
Iverson, R.M., 2000. Landslide triggering by rain infiltration. Water Resour. Res. 36 (7), 1897–1910. http://dx.doi.org/10.1029/2000wr900090.
Johnston, I., Murphy, W., Holden, J., 2021. A review of floodwater impacts on the stability of transportation embankments. Earth-Sci. Rev. 215, 103553. http://dx.doi.org/10.1016/j.earscirev.2021.103553.
Kang, S., Cho, S.E., Kim, B., Go, G.H., 2020. Effects of two-phase flow of water and air on shallow slope failures induced by rainfall: insights from slope stability assessment at a regional scale. Water 12 (3), http://dx.doi.org/10.3390/w12030812.
Kang, X., Yue, Z.Q., 2023. Flume test demonstration of landslide in stable gentle soil slope triggered by small mass of pressurized pore gas. Landslides 20 (12), 2635–2655. http://dx.doi.org/10.1007/s10346-023-02130-7.
Lei, X.Q., He, S.M., Abed, A., Chen, X.Q., Yang, Z.J., Wu, Y., 2021. A generalized interpolation material point method for modelling coupled thermo-hydro-mechanical problems. Comput. Methods Appl. Mech. Engrg. 386, 114080. http://dx.doi.org/10.1016/j.cma.2021.114080.
Lewis, R.W., Schrefler, B.A., 1998. The Finite Element Method in the Static and Dynamic Deformation and Consolidation of Porous Media. John Wiley & Sons, Chichester.
Liang, H.T., Wang, W., Wang, S.L., 2026. Experimental and numerical study of air–water two-phase flow in unsaturated loess with implications for slope stability. Catena 264 (109843), http://dx.doi.org/10.1016/j.catena.2026.109843.
Lu, N., Likos, W.J., 2004. Unsaturated Soil Mechanics. Wiley.
Ma, P.C., Ke, H., Lan, J.W., Chen, Y.M., He, H.J., 2019. Field measurement of pore pressures and liquid-gas distribution using drilling and ERT in a high food waste content MSW landfill in Guangzhou, China. Eng. Geol. 250, 21–33. http://dx.doi.org/10.1016/j.enggeo.2019.01.004.
Merry, S.M., Fritz, W.U., Budhu, M., Jesionek, K., 2006. Effect of gas on pore pressures in wet landfills. J. Geotech. Geoenvironmental Eng. 132 (5), 553–561. http://dx.doi.org/10.1061/(ASCE)1090-0241(2006)132:5(553).
Roth, G.A., Aydogan, F., 2015. Derivation of new mass, momentum, and energy conservation equations for two-phase flows. Prog. Nucl. Energy 80, 90–101. http://dx.doi.org/10.1016/j.pnucene.2014.12.007.
Schrefler, B.A., Scotta, R., 2001. A fully coupled dynamic model for two-phase fluid flow in deformable porous media. Comput. Methods Appl. Mech. Engrg. 190 (24–25), 3223–3246. http://dx.doi.org/10.1016/S0045-7825(00)00390-X.
Sheng, D., 2011. Review of fundamental principles in modelling unsaturated soil behaviour. Comput. Geotech. 38 (6), 757–776. http://dx.doi.org/10.1016/j.compgeo.2011.05.002.
Siemens, G.A., Peters, S.B., Take, W.A., 2013. Comparison of confined and unconfined infiltration in transparent porous media. Water Resour. Res. 49 (2), 851–863. http://dx.doi.org/10.1002/wrcr.20101.
Sun, X., Li, Y., Liu, Y., Song, Y., 2019. The effects of compressibility of natural gas hydrate-bearing sediments on gas production using depressurization. Energy 185, 837–846. http://dx.doi.org/10.1016/j.energy.2019.07.108.
Terzaghi, K., 1943. Theoretical Soil Mechanics. John Wiley & Sons, Inc, New York, http://dx.doi.org/10.1002/9780470172766.
Touma, J., Vauclin, M., 1986. Experimental and numerical analysis of two-phase infiltration in a partially saturated soil. Transp. Porous Media 1 (1), 27–55. http://dx.doi.org/10.1007/BF01036524.
Tracy, F.T., Vahedifard, F., 2022. Analytical solution for coupled hydro-mechanical modeling of infiltration in unsaturated soils. J. Hydrol. 612, 128198. http://dx.doi.org/10.1016/j.jhydrol.2022.128198.
van Bergeijk, V.M., 2022. Over the Dike Top: Modelling the Hydraulic Load of Overtopping Waves Including Transitions for Dike Cover Erosion (Ph.D. thesis). University of Twente, http://dx.doi.org/10.3990/1.9789036553414.
van Genuchten, M.T., 1980. A closed-form equation for predicting the hydraulic conductivity of unsaturated soils. Soil Sci. Am. J. 44 (5), 892–898. http://dx.doi.org/10.2136/sssaj1980.03615995004400050002x.
Wang, L., Nan, F.Y., Wang, S.M., Chen, Y., Li, X.W., Fan, Z.H., Chen, Y.S., 2023. Infiltration characteristics and deformation mechanism of rainfall-induced landslides in the three Gorges Reservoir Area based on 1D and 2D model tests. Rock Soil Mech. 44 (5), 1363–1374. http://dx.doi.org/10.16285/j.rsm.2022.00248.
Warmink, J.J., van Bergeijk, V., Chen, W., Aguilar-Lopez, J.P., Bomers, A., Hulscher, S.J.M.H., 2018. Modelling wave overtopping for flood defense reliability. In: Protections 2018: 3rd International Conference on Protection Against Overtopping. Grange-over-Sands, UK.
Weill, S., Mouche, E., Patin, J., 2009. A generalized Richards equation for surface/subsurface flow modelling. J. Hydrol. 366 (1–4), 9–20. http://dx.doi.org/10.1016/j.jhydrol.2008.12.007.
Whitaker, S., 1986. Flow in porous media I: a theoretical derivation of Darcy's law. Transp. Porous Media 1 (1), 3–25. http://dx.doi.org/10.1007/BF01036523.
Ye, Z., Wang, L., Zhu, B., Shao, H., Xu, W., Chen, Y., 2022. A thermo-hydro-chemo-mechanical coupled model for natural gas hydrate-bearing sediments considering gravity effect. J. Nat. Gas Sci. Eng. 108, 104823. http://dx.doi.org/10.1016/j.jngse.2022.104823.
Yerro, A., Alonso, E.E., Pinyol, N.M., 2015. The material point method for unsaturated soils. Geotechnique 65 (3), 201–217. http://dx.doi.org/10.1680/geot.14.P.163.
Yerro, A., Girardi, V., Martinelli, M., Ceccato, F., 2022. Modelling unsaturated soils with the material point method. A discussion of the state-of-the-art. Geomech. Energy Environ. 32, 100343. http://dx.doi.org/10.1016/j.gete.2022.100343.
Yu, J.D., Liang, W.J., Zhao, J.D., 2025. Enhancing dynamic modeling of porous media with compressible fluid: A THM material point method with improved fractional step formulation. Comput. Methods Appl. Mech. Engrg. 444, 118100. http://dx.doi.org/10.1016/j.cma.2025.118100.
Yu, J.D., Zhao, J.D., Liang, W.J., 2026. Multiscale modeling of coupled thermo-hydro-mechanical–chemical behavior in hydrate-bearing sediment. J. Mech. Phys. Solids 210, 106512. http://dx.doi.org/10.1016/j.jmps.2026.106512.
Yu, J.D., Zhao, J.D., Liang, W.J., Zhao, S.W., 2024. A semi-implicit material point method for coupled thermo-hydro-mechanical simulation of saturated porous media in large deformation. Comput. Methods Appl. Mech. Engrg. 418, 116462. http://dx.doi.org/10.1016/j.cma.2023.116462.
Zhang, X., Chen, Z., Liu, Y., 2017. Chapter 3 - the material point method. In: The Material Point Method. Academic Press, pp. 37–101. http://dx.doi.org/10.1016/B978-0-12-407716-4.00003-X.
Zhang, X.Y., Zhu, Y.M., Fang, C.H., 2009. The role of air flow in soil slope stability analysis. J. Hydrodyn. 21, 640–646. http://dx.doi.org/10.1016/S1001-6058(08)60195-X.
Zhou, G.G.D., Li, S., Lu, X., Tang, H., 2022. Large-scale landslide dam breach experiments: Overtopping and overtopping and seepage failures. Eng. Geol. 304, 106680. http://dx.doi.org/10.1016/j.enggeo.2022.106680.
Zienkiewicz, O.C., Shiomi, T., 1984. Dynamic behavior of saturated porous media: the generalized Biot formulation and its numerical solution. Int. J. Numer. Anal. Methods Geomech. 8 (1), 71–96. http://dx.doi.org/10.1002/nag.1610080106.